ADVANCING EARTH AND SPACE SCIENCES

JGR Oceans

RESEARCH ARTICLE
10.1029/2025JC023682

Key Points:
- Horizontal advection primarily determines sub-mesoscale salinity variability in the mixed layer of the northern Bay of Bengal
- The lateral salinity gradient determines sub-mesoscale density variations, with a characteristic space-time scale of about 15 km and 30 hr
- Relative cooling and warming between the barrier layer and the mixed layer determine the magnitude of temperature inversion

Supporting Information:
Supporting Information may be found in the online version of this article.

Correspondence to:
M. S. Girishkumar,
girish@incois.gov.in

Citation:
Thangaprakash, V. P., Girishkumar, M. S., Sreelekha, J., Sureshkumar, N., Shivaprasad, S., Ravichandran, M., et al. (2026). Investigating near-surface thermohaline structure and barrier layer temperature evolution in the northern Bay of Bengal using Seaglider and mooring observations in 2015. *Journal of Geophysical Research: Oceans*, *131*, e2025JC023682. https://doi.org/10.1029/2025JC023682

Received 31 OCT 2025
Accepted 22 JUN 2026

Author Contributions:
Conceptualization: V. P. Thangaprakash, M. S. Girishkumar
Data curation: V. P. Thangaprakash, J. Sreelekha, N. Sureshkumar, S. Shivaprasad
Formal analysis: V. P. Thangaprakash, M. S. Girishkumar, J. Sreelekha
Investigation: V. P. Thangaprakash
Methodology: V. P. Thangaprakash, M. S. Girishkumar
Project administration: M. Ravichandran, D. Sengupta
Supervision: M. Ravichandran, D. Sengupta, E. Pattabhi Rama Rao
Validation: V. P. Thangaprakash
Visualization: V. P. Thangaprakash
Writing – original draft: V. P. Thangaprakash

Investigating Near-Surface Thermohaline Structure and Barrier Layer Temperature Evolution in the Northern Bay of Bengal Using Seaglider and Mooring Observations in 2015

V. P. Thangaprakash[1,2], M. S. Girishkumar[1], J. Sreelekha[3], N. Sureshkumar[1], S. Shivaprasad[1], M. Ravichandran[1,4], D. Sengupta[5,6], J. T. Farrar[7], C. Lee[8], E. Pattabhi Rama Rao[1], S. S. V. S. Ramakrishna[2], and C. V. Naidu[2]

[1]Indian National Centre for Ocean Information Services, Hyderabad, India, [2]Department of Meteorology and Oceanography, Andhra University, Visakhapatnam, India, [3]Jet Propulsion Laboratory, California Institute of Technology, Pasadena, CA, USA, [4]Ministry of Earth Sciences, New Delhi, India, [5]International Centre for Theoretical Sciences, Bangalore, India, [6]Center for Geophysical Flows, Indian Institute of Technology Madras, Chennai, India, [7]Woods Hole Oceanographic Institution, Woods Hole, MA, USA, [8]Applied Physics Laboratory, University of Washington, Seattle, WA, USA

Abstract Concurrent vertical profiles of temperature and salinity with high temporal and spatial resolution from an underwater glider (Seaglider), along with near-surface meteorological and oceanographic parameters and subsurface currents measured by moorings, were used to quantify the various factors that modulated near-surface thermohaline structure in the northern Bay of Bengal (BoB) between 17 September and 6 December 2015. Sub-mesoscale filaments with characteristic spatial and temporal scales of approximately 15 km and 30 hr, respectively, were prevalent over the study region, with horizontal salinity gradient playing a substantial role in determining lateral density gradients. Mixed layer (ML) salinity variability was primarily determined by horizontal advection in the presence of strong horizontal salinity gradients, while vertical processes and local freshwater fluxes associated with precipitation events played a secondary roles. Although a barrier layer (BL) was present throughout the study period, temperature inversion was absent during the first half but was persistent and strong during the second half. Temperature budget analysis showed that the more pronounced cooling of the ML relative to the BL resulted from differences in effective heat flux and horizontal advection between the two layers, leading to the formation and strengthening of a temperature inversion during the second phase. In contrast, the absence of a temperature inversion during the first phase was attributed to comparable warming rates in both the ML and BL, resulting from the combined contributions of all the terms in the temperature budget.

Plain Language Summary The near-surface ocean in the northern Bay of Bengal exhibits a rich structure of small-scale lateral density features, particularly during the second half of the year due to the interaction between riverine freshwater input and mesoscale ocean eddies. Another consequence of this freshwater-induced near-surface salinity stratification is the formation of temperature inversions embedded within a thick barrier layer. In this study, we use high-resolution observations from a Seaglider and a mooring to estimate the characteristic spatial and temporal scales of these small-scale lateral density gradients and to examine the relative contributions of temperature and salinity to the associated density gradients. Our results show that lateral salinity gradients play the dominant role in controlling these features. The typical horizontal scale of these structures is approximately 15 km, and their characteristic time scale is about 30 hr. Taking advantage of the three-dimensional in situ observations obtained from the combined measurements of a mooring and a Seaglider, we further investigated the processes governing the formation of temperature inversions using mixed layer and barrier layer temperature budget analyses. The results show that stronger cooling of the mixed layer relative to the barrier layer primarily determines the magnitude of the temperature inversion.

1. Introduction

The Bay of Bengal (BoB) is a semi-enclosed basin in the north Indian Ocean, and the near-surface hydrographic state in this region plays a vital role in determining the weather and climate of the Indian subcontinent, which in turn impacts the livelihood of many people. The seasonal cycle of the near-surface hydrographic state in the BoB is primarily determined through the combined influence of local and remote forcings. The local forcing includes seasonally reversing monsoon winds, intense precipitation exceeding evaporation, and river discharge (Akhil

Writing – review & editing:
M. S. Girishkumar, D. Sengupta,
J. T. Farrar, C. Lee,
S. S. V. S. Ramakrishna, C. V. Naidu

et al., 2014; Ashin et al., 2019; Buckley et al., 2020; Chaitanya et al., 2021; Pant et al., 2015; Papa et al., 2010; Parampil et al., 2010; Pramanik et al., 2019; Prasad, 2004; Rao & Sivakumar, 2000, 2003; Sandeep et al., 2018; Sengupta et al., 2006, 2016; Shenoi et al., 2002; Sherin et al., 2023; Sree Lekha et al., 2018, 2020; Sreelekha & McPhaden, 2022). The remote forcing includes the generation of planetary waves in response to the modulation of winds over the equatorial Indian Ocean and the eastern BoB (Chen et al., 2018; Girishkumar, Ravichandran, & McPhaden, 2013; Li et al., 2017; Rao et al., 2010; Shankar et al., 2002; Yu et al., 1991).

A distinctive characteristic of the BoB, particularly in the northern Bay (nBoB), is that it is one of the freshest oceanic basins in the global tropics (Mahadevan et al., 2016; Figure 1a). This low salinity results from excess precipitation over evaporation and the influx of freshwater from the mighty Ganga-Brahmaputra-Meghna and Irrawaddy rivers (Chowdhury & Ward, 2004; Papa et al., 2010). In addition, the BoB also receives significant freshwater flux from the Godavari, Mahanadi, and Krishna rivers (Dai et al., 2009; Rao & Sivakumar, 2003; Sengupta et al., 2006) and this fresh water generally lies in the upper 30 m of the water column (Girishkumar et al., 2011; Thangaprakash et al., 2016, 2025; Vinayachandran et al., 2002; Wilson & Riser, 2016).

The low-salinity surface mixed layer (ML) often leads to the formation of a barrier layer (BL), which is sandwiched between the base of the salt-stratified mixed layer and the base of the isothermal layer (De Boyer Montégut et al., 2007; Girishkumar et al., 2011; Girishkumar, Ravichandran, & Han, 2013; Rao & Sivakumar, 2003; Thadathil et al., 2002, 2007; Thangaprakash et al., 2016; Vinayachandran et al., 2002). The barrier layer is often accompanied by inversions in the vertical temperature profile that are most pronounced in winter, with magnitudes occasionally reaching 4–5°C (Girishkumar, Ravichandran, & McPhaden, 2013; Thadathil et al., 2016; Thangaprakash et al., 2016). The riverine freshwater discharge into the nBoB contributes to distinct, large-scale lateral salinity gradients (Thangaprakash et al., 2025). The lateral stirring of low-salinity water from the north and relatively higher salinity waters by mesoscale eddies gives rise to sharp, salinity-dominated submesoscale fronts and filaments (Sengupta et al., 2016; Sree Lekha et al., 2018, 2020; Thangaprakash et al., 2025). In the past decade, extensive field measurements from ship-borne and autonomous instruments at sub-kilometer lateral resolution show that the central and nBoB are rich in submesoscale salinity-dominated fronts or filaments and three-dimensional frontal flows having typical spatial scales of 1–10 km and Rossby numbers nearly one (Adams et al., 2019; Lucas et al., 2016; MacKinnon et al., 2016; McKie et al., 2024; Ramachandran et al., 2018; Ramachandran & Tandon, 2020; Sengupta et al., 2016; Shroyer et al., 2016).

The shallow mixed layers, highly stratified halocline, and deep barrier layers in the nBoB affect the sea surface temperature (SST) and regional air-sea interaction, with significant impact on monsoon variability, tropical cyclone intensity, and ocean biogeochemistry (Girishkumar et al., 2017; Goswami, 2012; Li et al., 2017; Mahadevan et al., 2016; Orenstein et al., 2022; Pham et al., 2023; Prend et al., 2019; Sengupta & Ravichandran, 2001; Shroyer et al., 2021; Vecchi & Harrison, 2002). These hydrographic characteristics favor the rapid intensification of tropical cyclones (Balaguru et al., 2014; Chaudhuri et al., 2019; Lin et al., 2009; McPhaden et al., 2009; Sengupta et al., 2008) and have a significant influence on the biogeochemistry of the BoB (Gomes et al., 2000; Kumar et al., 2002).

However, despite extensive observations of submesoscale variability and strong salinity stratification in the nBoB, the processes that control the spatial decorrelation of SST and sea surface salinity (SSS), and the mechanisms that regulate the formation and variability of temperature inversions remain poorly constrained. This limitation arises in part from the lack of concurrent, high-resolution measurements that resolve both lateral gradients and vertical structure over sustained periods.

As part of the National Monsoon Mission project "Ocean Mixing and Monsoon" (OMM), a Seaglider (SG) equipped with temperature, conductivity, and biogeochemical sensors was deployed in the nBoB from 17 September to 6 December 2015 (SG15). During this mission, SG15 performed repeated butterfly patterns around the Woods Hole Oceanographic Institution (WHOI) mooring (18.01°N, 89.46°E; Weller et al., 2016) in the nBoB (Figure 1). The concurrent measurements of near-surface meteorological parameters, near- and sub-surface temperature, salinity, and currents from the WHOI mooring, in conjunction with high-resolution three-dimensional mapping of the temperature and salinity from SG15, enable us to quantify (a) the spatial and temporal decorrelation scales of SST and SSS and (b) the processes that modulate temperature inversion magnitude in the nBoB.

The paper is organized as follows. The data set and methodology are summarized in Section 2. The results are discussed in Section 3, and a summary of the results is presented in Section 4.

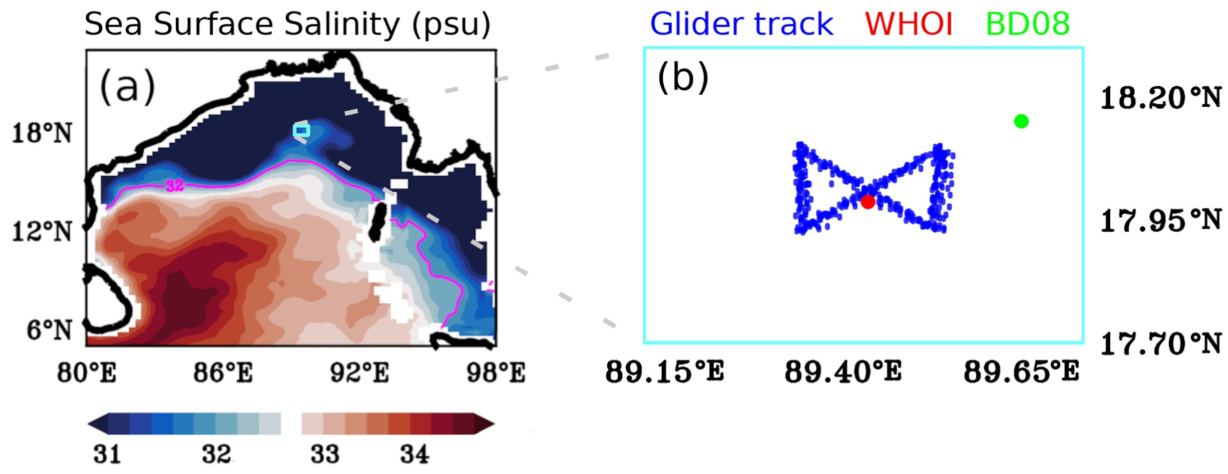

Figure 1. SMAP SSS (psu) averaged from September 2015 to December 2015. The pink contour represents the 32 psu isohaline, and the white box represents the Seaglider (SG15) survey site. (b) All SG15 measurement locations along the butterfly pattern from 17 September 2015 to 6 December 2015 in the northern BoB are shown (blue dots). The locations of the WHOI mooring at 18.01°N and 89.46°E (red closed circle) and the OMNI mooring BD08 at 17.83°N, 89.23°E (green closed circle) are marked.

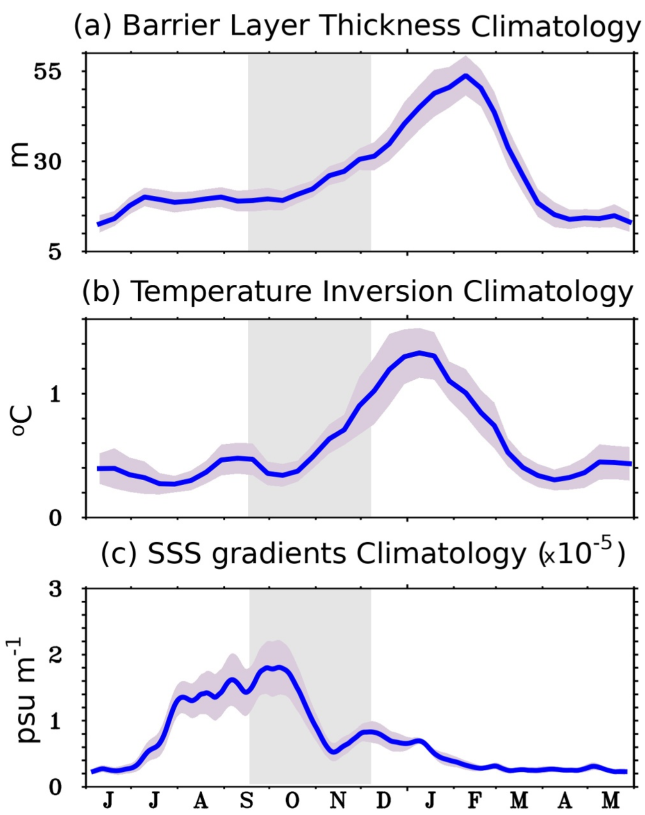

Figure 2. Climatological evolution of (a) BL thickness (m), (b) the magnitude of temperature inversion (°C); both estimated from the gridded Argo data with a 10-day temporal resolution and spatial resolution of 1°, and, (c) The lateral gradient of sea surface salinity (SSS; 10^{-5} psu m^{-1}) estimated from 8-day running mean gridded SMAP data with daily temporal and 25 km spatial resolution, and the SSS gradient is calculated as the centered difference (Δx and Δy are in 25 km) and averaged over the box (17°N–19°N, 88°E–90°E) at the SG15 survey site in the nBoB. The gray shading represents the SG15 survey period.

2. Data and Methods

2.1. Rationale for Selecting the SG15 Survey Period and Study Region

The glider survey site (18.01°N and 89.46°E) is located in the international waters, at the northernmost location in the nBoB. The climatological evolution of BL thickness, magnitude of temperature inversion (TI), and magnitude of near-surface lateral salinity gradient at the survey site showed prominent annual variability, that is, the magnitude of inversion peaks in December-January, while the barrier layer is thickest in January-February (Rao & Sivakumar, 2003; Thadathil et al., 2016; Thangaprakash et al., 2016; Figure 2). The glider survey period between September and December coincides with the growing phase of BL thickness and the magnitude of temperature inversion, from a minimum BL thickness and a weak temperature inversion in October to their maximum in February (Figures 2a and 2b). This timing provides an opportunity to distinguish the factors that determine the strength of temperature inversions during the thin and thick phases of the BL (Figures 2a and 2b). The concurrent measurements of surface meteorological parameters and sub-surface currents from the moorings, together with vertical profiles and lateral gradients of temperature and salinity from glider data, enable estimation of the individual components of the mixed layer and barrier layer temperature and salt budgets, and also to document the factors that modulate the magnitude of temperature inversion at daily time scales.

The glider survey period also coincides with the peak phase of annual variability of the lateral salinity gradient at the survey site (Figure 2c). The lateral SSS gradient associated with summer monsoon onset and the arrival of low-salinity water from the Ganga-Brahmaputra-Meghna river (Sree Lekha et al., 2020) intensifies in July, peaks in October, and decreases rapidly in November (Figure 2c). This seasonal evolution is consistent with Li et al. (2022). As a result, the SG15 survey also provides an opportunity to study the typical spatial and temporal scales of salinity and temperature gradients in the upper ocean, and their relative impact on density during the peak phase of the lateral SSS gradient.

Table 1
Vertical Resolution of Temperature and Salinity Sensors in the WHOI Mooring

Temperature: 0.5, 1, 2.3, 4, 5, 6, 8, 10, 14, 16, 18.3, 20, 23.6, 26, 28,42, 44, 48, 50, 52, 57.5, 60, 62.5, 67.5, 70, 76, 83.5, 89.5, 95.5, 104, 120, 135, 150, 175, and 200 m
Salinity: 1, 2.3, 5, 6, 10, 14, 18.3, 23.6, 26, 42, 44, 48, 50, 52, 57.5, 60, 70, 76, 83.5, 89.5, 95.5, 104, 120, 150, and 200 m

2.2. Data

2.2.1. Seaglider

Temperature and salinity were measured by a Seaglider (designated "SG15") using Sea-Bird Conductivity-Temperature (CT) sensors operating in free-flow mode (unpumped) with accuracies of ±0.0003 S m^{-1} and ±0.002°C, respectively. Chlorophyll concentrations at an accuracy of ±0.015 mg m^{-3}, measured using a WETLabs Eco Puck sensor on the glider, were used to estimate light attenuation. The glider also measured other biogeochemical parameters, but these data are not used here. Although the Seaglider collected data down to 1,000 m, the present analysis is restricted to the upper 150 m because both the mixed layer and the barrier layer are confined to this depth range.

SG15 performed 12 butterfly patterns around the WHOI mooring at 18.01°N, 89.46°E during the mission from 17 September to 6 December 2015, with the zonal and meridional transects of each pattern being about 22 km (Figure 1). The glider took approximately 5–6 days to complete each butterfly pattern, typically traveling about 88 km. The standard data quality control procedure proposed by Schmid et al. (2007) and UW (2013) was applied to the raw glider temperature and salinity data. This quality-control approach reduces outliers, mitigates sensor lag effects, minimizes directional flow bias, and ensures stable and physically consistent vertical density structure.

The Seaglider covered a lateral distance of about 3 km in 5 hr, and measurements were collected during both downward and upward casts up to 1,000 m depth. Given its vertical speed of 0.17 m/s, the glider would take approximately 15 min to traverse a depth of 150 m. Hence, the typical time for an upcast (150–0 m) followed by a downcast (0–150 m) is approximately 30 min; these two profiles represent a quasi-synoptic snapshot of the upper-ocean hydrographic state (Figure S1 in Supporting Information S1). Upcast and downcast data were first averaged independently within 1 m bins, and missing values at specific depths were filled using linear interpolation. The interpolated upcast and downcast profiles were then averaged to produce a single consolidated profile (Hauri et al., 2024). In this study, consecutive upcast and downcast profiles were averaged up to a depth of 150 m (rather than pairing profiles across longer time intervals) to minimize temporal offsets.

2.2.2. Moorings

Surface meteorological measurements and near-surface ocean temperature and salinity from the WHOI mooring are used in this analysis. Vertical profiles of currents were obtained using a 1,000 kHz Nortek Aquadopp Acoustic Doppler Current Profiler (ADCP) at 6 m, 8 m, and 10 m, along with single-point Doppler current meters deployed at 3.5 m (Nortek Aquadopp) and 11 m (Aanderaa Seaguard RCM) on the WHOI mooring. The depths of temperature and salinity measurements from Seabird sensors (SBE39 and SBE37) on the WHOI mooring are listed in Table 1. The WHOI mooring was equipped with an ASIMET system that measured near-surface meteorology, including wind speed and direction, barometric pressure, air temperature, relative humidity, precipitation, downwelling shortwave radiation, and downwelling longwave radiation, at a height of 3 m above the sea surface (Weller et al., 2016, 2019). The meteorological measurements have a temporal resolution of 1 minute, the temperature and salinity measurements have a nominal resolution of 5 min (with some variation between instrument types), and the velocity measurements have a resolution of 1 hr. In addition, the vertical profile of ocean current velocity from 15 to 105 m in 5 m bins from a downward-looking 300 kHz RDI ADCP mounted at 7.5 m depth on the Ocean Moored Buoy Network for Northern Indian Ocean (OMNI) BD08 mooring at 18.15°N, 89.67°E, maintained by the National Institute of Ocean Technology (NIOT) is also used to complement the analysis (Venkatesan et al., 2013). The temporal resolution of current data from the OMNI mooring is 1 hr.

2.2.3. Satellite and Gridded Data Products

The optimally interpolated 8-day running average of Soil Moisture Active Passive (SMAP) SSS data with 25-km spatial and daily temporal resolution (Meissner et al., 2022) is used to describe the spatio-temporal evolution of near-surface salinity characteristics over the BoB. The Advanced Scatterometer (ASCAT) wind vectors with 25 km spatial and daily temporal resolution (Bentamy & Fillon, 2012) are used to estimate Ekman pumping velocity (Girishkumar, Ravichandran, & McPhaden, 2013; Yu, 2003). Merged-gridded sea surface height anomaly (SSHA) data from multi-altimeter missions (CMEMS) are used to characterize the westward propagating mesoscale features in the nBoB during the study period. Gridded temperature and salinity data with 1° spatial resolution and 10-day temporal resolution are derived from Argo profiles using Data Interpolation Variational Analysis (DIVA) is used to describe climatological hydrographic conditions in the study region (Jha & Udaya Bhaskar, 2021). These data are gridded at depths of 5, 10, 20, 30, 50, 75, 100, and 125 m.

2.3. Methods

2.3.1. Mixed Layer Depth, Isothermal Layer Depth, Barrier Layer, and Temperature Inversion

The mixed layer depth (MLD) is defined as the depth at which density equals the sea surface density ($\sigma_{t(z=0)}$) plus an increment in density ($\Delta\sigma_t$) of magnitude 0.125 kg m^{-3} (Girishkumar, Ravichandran, & McPhaden, 2013; Kara et al., 2003; Sreelekha & McPhaden, 2022). Consistent with this definition, the isothermal layer depth (ILD) is defined as the depth where the temperature is 0.5°C lower than the SST. The ILD criterion used in the present study is consistent with the density criteria used to estimate MLD; when vertical salinity stratification is negligible, the MLD and ILD are identical (Girishkumar, Ravichandran, & McPhaden, 2013).

The region between MLD and ILD is defined as the barrier layer; the difference between ILD and MLD is defined as barrier layer thickness. A temperature inversion is identified when the water temperature at depth is higher than SST by at least 0.1°C, and the difference between the maximum subsurface temperature and SST defines the magnitude of temperature inversion (TI) (Girishkumar, Ravichandran, & Han, 2013; Thadathil et al., 2002; Thangaprakash et al., 2016).

2.3.2. Horizontal Turner Angle (Tu_H)

Following Rudnick and Martin (2002) and Cole et al. (2010), the relative contribution of spatial variation of salinity and temperature gradients on the lateral variation of density changes in the mixed layer along the glider transect is evaluated using horizontal Turner Angle (Tu_H) and it is defined as $Tu_H = \tan^{-1}(\alpha\Delta T + \beta\Delta S, \alpha\Delta T - \beta\Delta S)$; where α and β denote the coefficients of thermal expansion and haline contraction, with approximate values of 3.2×10^{-4}°C^{-1} and 7.35×10^{-4} kg g^{-1}, respectively. ΔT and ΔS are lateral gradients in mixed layer temperature and salinity computed along the glider track. Tu_H values between −45° and 45° imply that the contribution from the temperature and salinity together determines density, with an equal contribution from temperature and salinity at 0°. When the Tu_H value approaches 45°, it implies that temperature is the sole contributor to horizontal density variation. In contrast, when Tu_H value approaches −45°, indicating that salinity is the primary contributor to density changes. Tu_H values between 45° and 90° indicate salinity opposing the density changes due to temperature, and Tu_H values between −90° and −45° indicate temperature working against density changes due to salinity variability. $|Tu_H| > 90°$ indicates an unstable regime, which is excluded from this analysis.

2.3.3. Spatial and Temporal Decorrelation Length Scale

The characteristics of spatial and temporal scale variability of SSS and SST at the survey site are examined using spatial and temporal decorrelation scales. Temporal decorrelation scales quantify the persistence of SST and SSS signals, whereas the spatial decorrelation length scale provides some insight into the nature and spatial extent of the variability, in particular the contribution from sub-mesoscale processes. As noted earlier, the glider covers a total distance of about 88 km in each butterfly pattern, and the effective spatial and temporal resolution of the glider data is about 3 km and 5 hr. The spatial and temporal decorrelation scales are estimated as the distance (or time) at which the lagged autocorrelation falls by a factor e^{-1} (∼0.37) of its value at zero lag (i.e., 1.0).

Diurnal variability of SST in response to the diurnal cycle of solar radiation is an energetic signal in the record. Since our main interest here is the variability associated with other ocean dynamical processes, we have removed the bandpass diurnal signals (24 ± 3 hr) using a harmonic filter from the mooring and Seaglider data before estimating Tu_H, spatial decorrelation length, and time scales.

2.3.4. Mixed Layer Temperature and Salinity Budget

Following Rao and Sivakumar (2003), Girishkumar, Ravichandran, & McPhaden (2013), and Thangaprakash et al. (2016, 2025), the mixed layer temperature and salinity budgets are estimated using the following equations.

$$\frac{\partial T_{\mathrm{ML}}}{\partial t} = \frac{Q_{\mathrm{EF\_ML}}}{\rho C_p \mathrm{MLD}} - \left[\left(u_{\mathrm{ML}}\frac{\partial T_{\mathrm{ML}}}{\partial x} + v_{\mathrm{ML}}\frac{\partial T_{\mathrm{ML}}}{\partial y}\right) + \left(\frac{\partial \mathrm{MLD}}{\partial t}\right)\left(\frac{T_{\mathrm{ML}} - T_{\mathrm{MLD+5\,m}}}{\mathrm{MLD}}\right)\right] + \mathrm{Residual} \quad (1)$$

$$\frac{\partial S_{\mathrm{ML}}}{\partial t} = \frac{(E-P)\,S_{\mathrm{ML}}}{\mathrm{MLD}} - \left[\left(u_{\mathrm{ML}}\frac{\partial S_{\mathrm{ML}}}{\partial x} + v_{\mathrm{ML}}\frac{\partial S_{\mathrm{ML}}}{\partial y}\right) + \left(\frac{\partial \mathrm{MLD}}{\partial t}\right)\left(\frac{S_{\mathrm{ML}} - S_{\mathrm{MLD+5\,m}}}{\mathrm{MLD}}\right)\right] + \mathrm{Residual} \quad (2)$$

The individual terms in Equation 1 from left to right represent mixed layer temperature tendency, effective surface heat flux ($Q_{\mathrm{EF\_ML}}$) in the mixed layer, horizontal advection, vertical processes and residual. Similarly, the terms in Equation 2 represent mixed layer salinity tendency, local freshwater flux due to evaporation (E) and precipitation (P), horizontal advection, vertical processes, and residual.

In Equations 1 and 2, T_{ML} is the mixed layer averaged temperature, S_{ML} is the mixed layer averaged salinity, t is the time (in days), C_p is the specific heat capacity of seawater (3993 J kg^{-1} K^{-1}), and ρ is the density of seawater (1,024 kg m^{-3}). $\frac{\partial T_{\mathrm{ML}}}{\partial x}$ and $\frac{\partial T_{\mathrm{ML}}}{\partial y}$, $\frac{\partial S_{\mathrm{ML}}}{\partial x}$ and $\frac{\partial S_{\mathrm{ML}}}{\partial y}$ are zonal and meridional gradients of mixed layer averaged temperature and salinity, respectively. The u_{ML} and v_{ML} are the zonal and meridional components of the current, respectively, averaged over the mixed layer and estimated from the WHOI mooring. $\frac{\partial \mathrm{MLD}}{\partial t}$ is the entrainment/detrainment velocity associated with the deepening and shallowing phase of the mixed layer (Kim et al., 2006; Sherin et al., 2023), estimated as the rate of change of MLD (m day^{-1}). $T_{\mathrm{MLD+5\ m}}$ and $S_{\mathrm{MLD+5\ m}}$ represent the temperature and salinity at 5 m below the mixed layer that are entrained and detrained into the mixed layer during its deepening and shallowing phase (Thangaprakash et al., 2016, 2025).

The effective surface heat flux available in the mixed layer ($Q_{\mathrm{EF\_ML}}$) is estimated after subtracting the penetrative component of shortwave radiation (Q_{pen}) just below the MLD from the net surface heat flux (Q_{net}). The Q_{net} is the sum of net shortwave radiation (NSW), net longwave radiation (NLW), latent heat flux (LHF) and sensible heat flux (SHF).

An albedo correction of 0.945 is applied to downwelling shortwave radiation from the mooring to estimate the NSW at the sea surface. The net longwave radiation (NLW) at the sea surface is estimated from buoy-measured downwelling longwave radiation (DWL) and SST using Equation 3.

$$\mathrm{NLW} = 0.97 * \left(\sigma * (\mathrm{SST} + 273.15)^4 - \mathrm{DWL}\right) \quad (3)$$

Where σ represents the Stefan-Boltzmann constant (5.67 × 10^{-8} W m^{-2} K^{-4}). The latent and sensible heat flux is estimated with meteorological and near-surface oceanographic parameters from the mooring using the Coupled Ocean-Atmosphere Response Experiment (COARE) Version 3.0 bulk flux algorithm (Fairall et al., 2003; Weller et al., 2016).

The Q_{pen} at the base of the mixed layer was estimated using a double exponential expression proposed by Morel and Antoine (1994).

$$Q_{\mathrm{pen}} = 0.43 * \mathrm{NSW}\left[V_1 e^{-\mathrm{MLD}/\xi_1} + V_2 e^{-\mathrm{MLD}/\xi_2}\right] \quad (4)$$

In Equation 4, the value 0.43 indicates the fraction of incident NSW at the surface that penetrates below 2 m depth. V_1, V_2, ζ_1, and ζ_2 values are estimated from chlorophyll measurements (mg m^{-3}) at 4 m from SG15 using the expression proposed by Sweeney et al. (2005). V_1 and V_2 represent the fraction of the long-visible and short-visible/ultraviolet wavelengths at the surface; ζ_1 and ζ_2 are the attenuation depths of long-visible and short-visible/ultraviolet wavelengths.

The Q_{pen} is sensitive to the choice of the attenuation coefficients. Whenever MLD becomes too shallow, the resultant Q_{pen} is too divergent. However, our choice of estimating attenuation depths of long-visible (ζ_1) and short-visible/ultraviolet wavelengths (ζ_2) using a double exponential expression proposed by Morel and Antoine (1994) in this study is found to be 1.5 and 21 m, respectively, which is close to the earlier studies with mean attenuation depths of 0.9 ± 0.4 m and 20.8 ± 0.6 m, respectively (Lotliker et al., 2016).

Precipitation is estimated from mooring measurements, and evaporation is estimated using the expression, $E = Q_L L_v^{-1} \rho^{-1}$, Where Q_L is the latent heat flux and L_v is the latent heat of vaporization, taken as 2.44×10^6 J kg^{-1}.

We used daily averaged WHOI mooring data to estimate all the terms in the mixed layer temperature and salinity budget, except for the spatial temperature and salinity gradient. The zonal and meridional gradient of temperature ($\frac{\partial T_{ML}}{\partial x}$ and $\frac{\partial T_{ML}}{\partial y}$) and salinity ($\frac{\partial S_{ML}}{\partial x}$ and $\frac{\partial S_{ML}}{\partial y}$) averaged over the mixed layer is estimated from gridded SG15 temperature and salinity data with a spatial resolution of 0.01° (~1 km), ~1 m vertical resolution, and daily temporal resolution. The scattered measurements from glider observations were converted to a regular grid using the following approach. Glider data collected within 3 days before and after a given target day were combined to generate a scattered spatial map for that day. For each cycle, the scattered observations were interpolated onto a regular 1 km × 1 km grid using a spline-smoothed Laplacian interpolation with appropriate weighting to reduce noise while preserving the overall butterfly structure. Interpolation was restricted to grid points within five grid cells (~5 km) of an observation to ensure reliable coverage, particularly near the edges of the features.

After gridding the glider measurements, we choose temperature and salinity values separated by 8 km across the WHOI mooring along zonal and meridional directions to estimate the horizontal gradient of temperature and salinity. The MLD was deeper than 11 m during 65% of the study period; therefore, the velocity measurements between 6 and 11 m from the WHOI mooring are considered representative of the mixed layer averaged currents. The zonal and meridional gradients estimated from glider and current measurements from WHOI moorings were used to estimate horizontal advection. Since the mixed layer temperature and salinity budget were calculated using daily averaged data, variability with timescales shorter than 24 hr was filtered out from the glider and mooring data before estimating the budget.

2.3.5. Barrier Layer Temperature Budget

The following equation was used to estimate the barrier layer temperature budget.

$$\frac{\partial T_{BL}}{\partial t} = \frac{Q_{EF\_BL}}{\rho C_p\,(\mathrm{ILD}-\mathrm{MLD})} - \left[\left(u_{BL}\frac{\partial T_{BL}}{\partial x} + v_{BL}\frac{\partial T_{BL}}{\partial y}\right)\right] + \left[\left(\frac{\partial \mathrm{MLD}}{\partial t}\right)\left(\frac{T_{BL}-T_{ML}}{\mathrm{ILD}-\mathrm{MLD}}\right) + \left(\frac{\partial \mathrm{ILD}}{\partial t}\right)\left(\frac{T_{BL}-T_{BL+5\,m}}{\mathrm{ILD}-\mathrm{MLD}}\right)\right] + \mathrm{Residual} \tag{5}$$

The individual terms in Equation 5 from left to right represent barrier layer temperature tendency, effective heat flux available in the barrier layer (Q_{EF_BL}) after accounting for the difference of Q_{pen} across the MLD and the ILD, horizontal advection, vertical processes, and residual terms.

In Equation 5, T_{BL} is the temperature averaged over the barrier layer, ILD-MLD is the barrier layer thickness in *m*, $\frac{\partial \mathrm{MLD}}{\partial t}$ and $\frac{\partial \mathrm{ILD}}{\partial t}$ is the entrainment/detrainment velocity at the top and bottom of the barrier layer, estimated as the rate of change of MLD (m day^{-1}) and rate of change of ILD (m day^{-1}), respectively. $T_{BL+5\,m}$ represents the magnitude of temperature at 5 m below the isothermal layer (base of barrier layer) that is entrained/detrained into the barrier layer during the deepening/shallowing phase of the Isothermal layer.

The current measurements below 11 m depth are not available from the WHOI mooring; hence, the sub-surface current measurements between 15 and 105 m from the BD08 mooring (located approximately 28 km from the WHOI mooring) are used to estimate u_{BL} and v_{BL} in Equation 5. Similar to the mixed layer temperature budget, the zonal and meridional temperature gradients in the barrier layer are estimated from the gridded SG15 temperature field, as mentioned in Section 2.3.4.

Measurement errors associated with instrumentation, sampling, schemes used for parameterization, finite differencing, and the exclusion of the horizontal and vertical diffusion terms in our budget equations are included in the residual (Vialard et al., 2008).

3. Results and Discussion

We first describe the near-surface atmospheric conditions in the northern BoB during the study period to set the stage for the subsequent analysis (Section 3.1). We then examine the temporal and spatial scales of small-scale near-surface lateral density gradient features, along with the relative roles of salinity and temperature gradients in their variability (Section 3.2). Next, we analyze the factors controlling mixed layer temperature and salinity using the respective mixed layer temperature and salinity budgets (Sections 3.3, 3.4, and 3.5). Finally, we investigate the processes modulating the magnitude of temperature inversion using both the mixed layer and barrier layer temperature budgets (Section 3.5.3).

3.1. Near-Surface Atmospheric Conditions

The near-surface atmosphere exhibits distinct characteristics in the first and second halves of the SG15 survey period (Figure 3). The wind speed was relatively weak (∼3 m s^{-1}) and varied in direction during the first half (September–October) of the survey, whereas the winds were stronger (4–6 m s^{-1}) and predominantly from the northeast during the latter half (November to December; Figures 3a and 3b). The temporal evolution of the wind speed and direction during the SG15 survey is consistent with climatological winds in the nBoB between the fall inter-monsoon and winter monsoon (Hastenrath, 1994; Thangaprakash et al., 2016).

Climatologically, the onset of northeasterly wind at the end of the calendar year reduces air temperature (AT) and relative humidity (RH) in response to the intrusion of dry and cold continental air into the BoB (Rao & Sivakumar, 2000; Thangaprakash et al., 2016). These characteristics are evident during the survey period (Figures 3c and 3d). AT and RH are higher (∼28.7°C and ∼80%) during the first half than in the second half of the survey (∼27.5°C and ∼74%; Figures 3c and 3d). The decrease of specific humidity (from 20 g kg^{-1} to 17 g kg^{-1}) and increase of sea-air specific humidity difference (q_s–q_a; from 5 g kg^{-1} to 7 g kg^{-1}), together with a slight increase of wind speed, leads to an increase in the magnitude of LHF during the second half of the survey (−120 Wm^{-2}) relative to the first half (−80 Wm^{-2}; Figures 3e and 3h). The negative and positive values of radiative and turbulent heat flux indicate heat loss from the ocean and gain by the ocean, respectively. Enhancement in SHF loss from −4 to −7 W m^{-2} is also apparent in response to increasing wind speed and enhanced sea-air temperature differences during the second phase (Figure 3i). NLW varies between −45 and −60 W m^{-2} during the survey period, with reduced NLW from the ocean surface in cloudy and rainy conditions (Figure 3j). NSW at the sea surface gradually decreases during the survey, from 210 W m^{-2} to nearly 160 Wm^{-2} (Figure 3k), as may be expected during the transition from summer to winter.

These variations in radiative and turbulent fluxes resulted in a net surface heat gain by the ocean during the first half of the survey, while the second half exhibited modulation between small positive and negative fluxes (Figure 3l). The average value of net surface heat flux during the first half of the survey period is around 70 W m^{-2}, compared to −20 W m^{-2} in the second half. After adjusting the net surface heat flux to account for the penetration of shortwave radiation below the mixed layer (∼15%), the ocean mixed layer gained approximately 40 W m^{-2} in the first half, in contrast to a heat loss of about −40 W m^{-2} during the second half (Figure 3l; red line).

Isolated short-lived rainfall events (0.8 mm hr^{-1} to 2 mm hr^{-1}) were observed, particularly during the first half of the survey period (Figure 3g). These events significantly reduce the net surface heat flux at the sea surface or occasionally reverse the sign compared to the slowly evolving prevailing background conditions (Figure 3l). For instance, the difference in net surface heat flux immediately before the 7-day rain event at the end of October and the minimum value during the event is nearly −200 W m^{-2}. A comparison of the radiative and turbulent heat fluxes with net surface heat flux indicates that the reduction is primarily associated with the enhancement of LHF and reduction in NSW (Figure 3). Previous studies in the BoB show that the reduction in the LHF during these rainfall events is due to the generation of the atmospheric cold pools, triggered by downdrafts from convective systems and reduced NSW at the sea surface due to cloud cover (Girishkumar et al., 2021; Jofia et al., 2021; Simoes-Sousa et al., 2022).

3.2. Spatial and Temporal Decorrelation Scale of SST and SSS

The horizontal variations of SST and SSS along the glider track during four representative butterfly patterns from the SG15 survey are depicted in Figure 4a. Within the ∼22 km span of each track, SST, SSS and surface σ_t exhibit

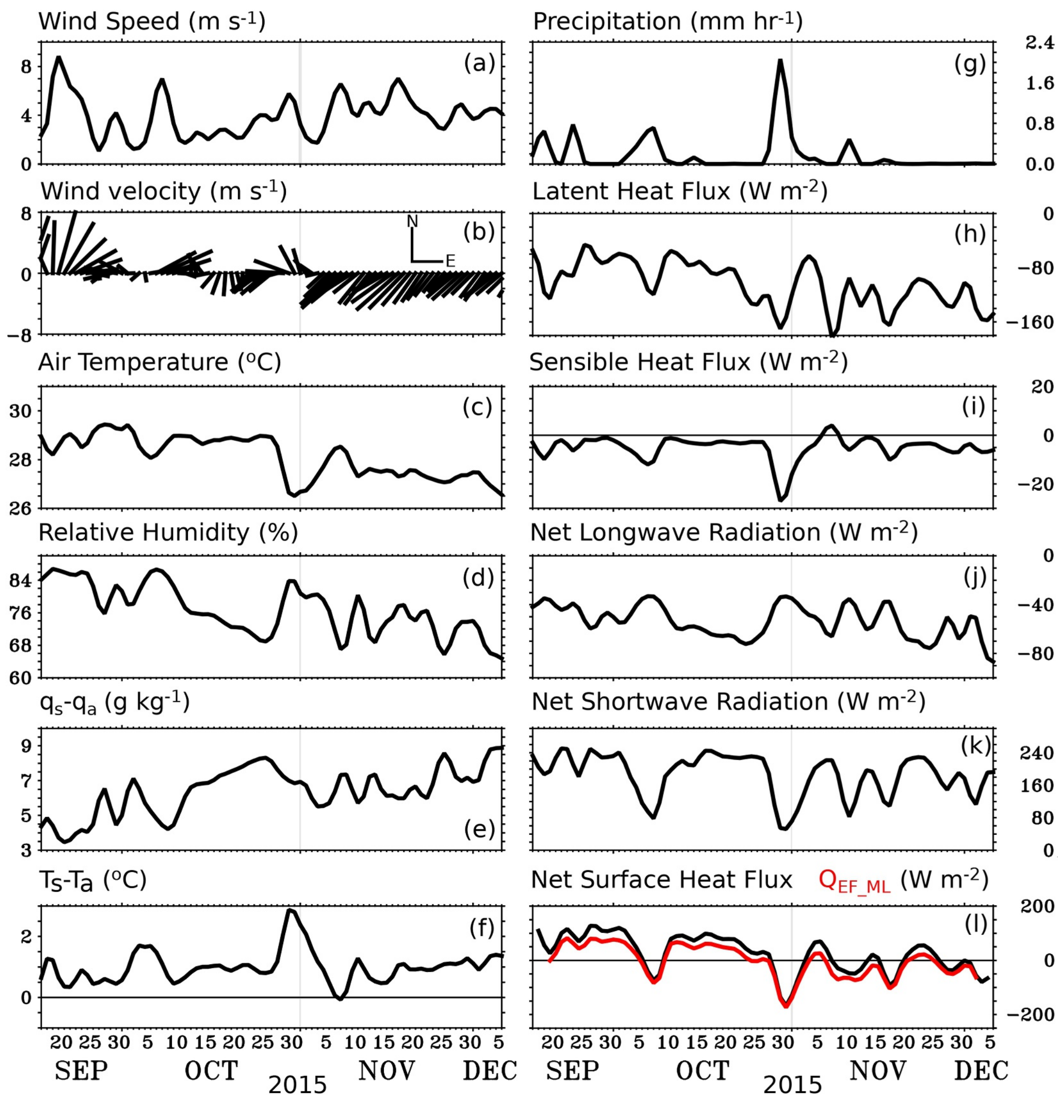

Figure 3. Temporal evolution of daily average of meteorological parameters (a) wind speed (ms^{-1}), (b) wind vectors (ms^{-1}), (c) air temperature (°C), (d) relative humidity (%), (e) specific humidity difference between sea and air (q_s−q_a; g kg^{-1}), (f) temperature difference between sea and air (T_s−T_a, °C), (g) precipitation (mm hr^{-1}), (h) latent heat flux (Wm^{-2}), (i) sensible heat flux (Wm^{-2}), (j) net longwave radiation (Wm^{-2}), (k) net shortwave radiation (Wm^{-2}), (l) net surface heat flux (Wm^{-2}; black) and effective heat flux available in the mixed layer (Wm^{-2}; red) derived from WHOI mooring at 18.01°N, 89.46°E from 17 September to 6 December 2015. The gray vertical line (on 30 October 2015) demarcates the transition between the first and second half of the SG15 study period. The negative and positive values of radiative and turbulent heat flux indicate heat loss from the ocean and gain by the ocean, respectively.

pronounced lateral variability. For individual butterfly patterns, the difference between the minimum and maximum values ranges from ~0.3 to 1.4°C for SST, ~0.6 to 2.6 psu for SSS and ~0.5 to 1.7 kg m^{-3} for surface σ_t (Figure S2 in Supporting Information S1).

To examine the relative contributions of horizontal temperature and salinity gradients to the horizontal density gradient, frequency histograms of $\alpha\partial\theta/\partial s$ and $\beta\partial S/\partial s$ were calculated using mixed layer averaged potential temperature and salinity (where s denotes the horizontal distance between two observation points, $\partial\theta/\partial s$ and $\partial S/\partial s$ represents horizontal temperature and salinity gradients, respectively). The temperature and salinity gradients were multiplied by the thermal expansion coefficient (α) and haline contraction coefficient (β), respectively, to scale their contributions to the density gradient. This scaling enables a direct comparison of the relative roles of temperature and salinity in determining the horizontal density gradient (Pickard & Emery, 1990).

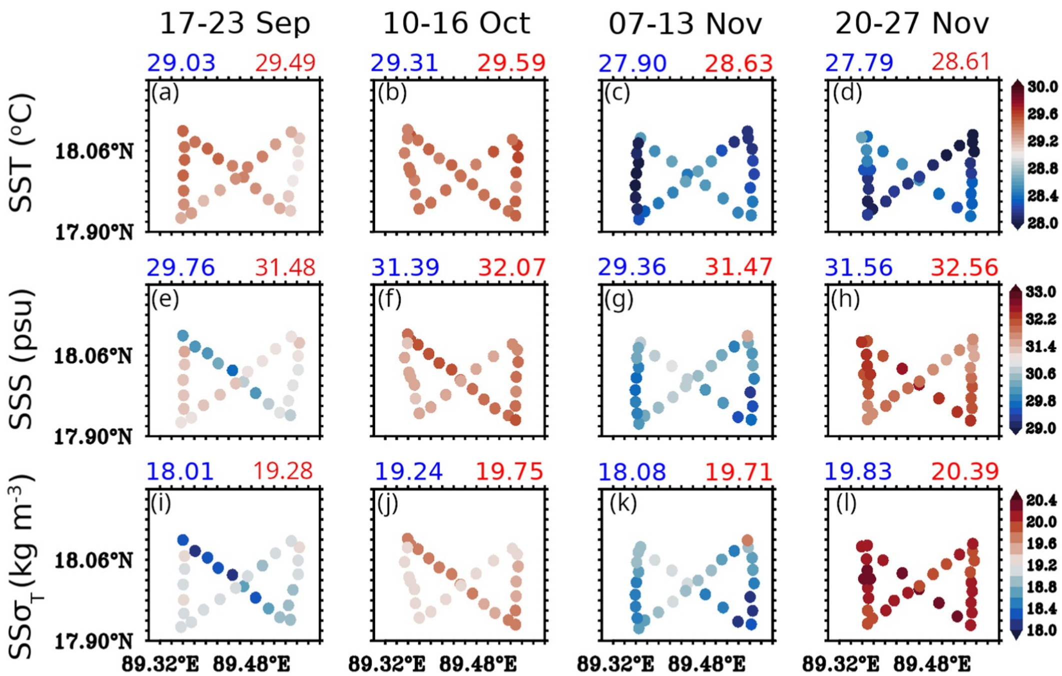

Figure 4. (a–d) SST (°C), (e, f, g, and h) SSS (psu) and (i–l) surface σ_t (kg m^{-3}) along the four representative SG15 butterfly patterns during (a, e, and i) 17–23 September 2015, (b, f, and j) 10–16 October 2015, (c, g, and k) 07–13 November 2015, (d, h, and l) 20–27 November 2015. The numbers at the top of each panel represent the minimum (blue) and maximum (red) values of the respective parameters during that particular butterfly survey.

Further analysis of frequency histograms of the magnitudes of horizontal gradients of mixed layer averaged temperature and salinity shows that approximately 61% of the $\beta\partial S/\partial s$ values exceed 0.1×10^{-4} km^{-1}, whereas only 15% of the $\alpha\partial\theta/\partial s$ values exceed 0.1×10^{-4} km^{-1} (Figure 5). Similarly, $\beta\partial S/\partial s$ values greater than 0.2×10^{-4} km^{-1} occur about 42% of the time, while $\alpha\partial\theta/\partial s$ exceeds 0.2×10^{-4} km^{-1} only 4% of the time (Figure 5). The percentage of values exceeding these arbitrarily selected thresholds is higher for $\beta\partial S/\partial s$ than for $\alpha\partial\theta/\partial s$, indicating that the horizontal density gradient is primarily determined by the horizontal salinity gradient (Figure 4). This is further corroborated by using Tu_H (Figure 5d).

The frequency histogram of Tu_H estimated using the mixed layer averaged temperature and salinity shows that approximately 85% of Tu_H values lie between −90° and 0, and of these, approximately 54% of Tu_H fall between −90° and −45°, implying the predominant role of horizontal salinity gradient in determining the lateral density changes (Figure 5). As a result, it is apparent that there is marked spatial correspondence between horizontal variability of salinity and density along the SG15 survey path (Figure 4; see panels e and i, panels g and k). In summary, horizontal salinity gradients occur more frequently and contribute more strongly to horizontal density structure than temperature gradients within the mixed layer.

To evaluate how deeply the salinity-controlled lateral density gradients dominate, we examined the frequency distribution of Tu_H at 30 m (just below the mixed layer), 50 m (upper thermocline), and 75 m (within the thermocline; Figure 5). As depth increases, the Tu_H clusters toward 45°, indicating that horizontal salinity gradients have less influence on lateral density gradients at deeper depths, and that lateral density variability at these depths is increasingly determined by temperature gradients. Consistently, the values of $\beta\partial S/\partial s$ restricted to smaller values compared to $\alpha\partial\theta/\partial s$ as depth increased in contrast to the mixed layer (Figure 5). Thus, the dominant role of salinity in controlling lateral density gradients is confined to the mixed layer.

The lagged spatial autocorrelation of glider SST, SSS, and surface σ_t along individual butterfly patterns depicts that the typical spatial scales of these parameters vary between 4–31 km, 8–51 km, and 8–52 km, with mean values of 11 km, 16 km, and 16 km, respectively (Figures 6d–6f). Similarly, the lagged temporal autocorrelation of mooring SST, SSS, and surface σ_t indicates temporal scales varying from 5–54 hr, 12–85 hr, and 19–79 hr, with mean values of 17 hr, 27 hr, and 31 hr, respectively (Figures 6a–6c). These length scales are distinctly smaller than

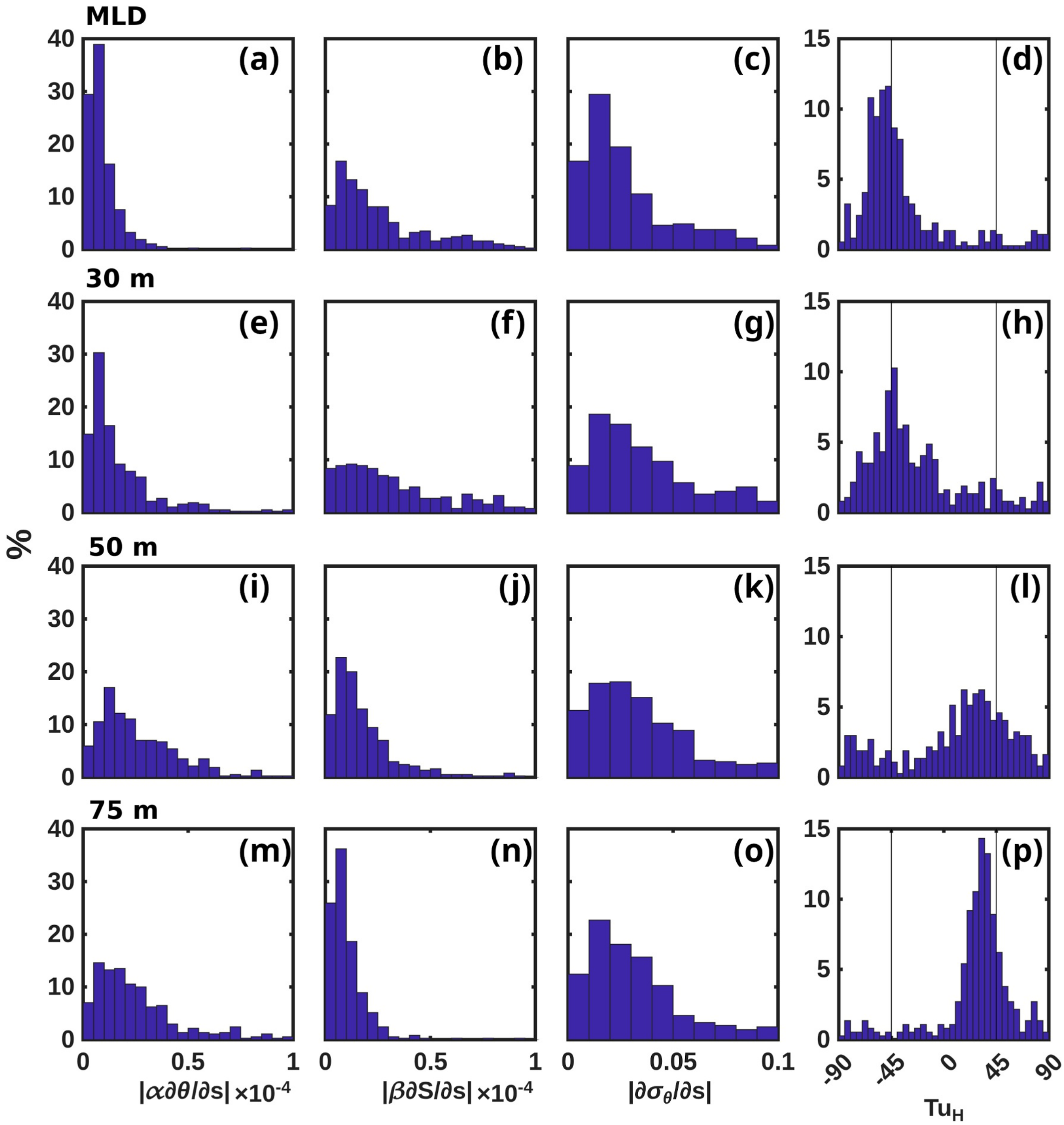

Figure 5. Frequency histogram (in %) of (a, e, i, and m) $\left|\alpha \frac{\partial \theta}{\partial s}\right|$ ($\times 10^{-4}$ km^{-1}), (b, f, j and n) $\left|\beta \frac{\partial S}{\partial s}\right|$ ($\times 10^{-4}$ km^{-1}), (c, g, k, and o) potential density ($\left|\frac{\partial \sigma_\theta}{\partial s}\right|$; kg m^{-3} km^{-1}) and (d, h, l, and p) horizontal Turner Angle (Tu_H; °) derived from the SG15 survey track during the period from 17 September to 06 December 2015 using the data (a–d) averaged over the mixed layer, (e–h) at 30 m (below the mixed layer), (i–l) 50 m (upper thermocline) and (m–p) 75 m (from the middle of thermocline). The number of data points to construct the histogram in each panel is 256.

the Rossby radius of deformation at 18°N (~60 km; Chelton et al., 1998), and the temporal scales are shorter than those associated with mesoscale eddies or Rossby waves, which move westward at a theoretical speed of 4.3 cm s^{-1} at these latitudes (Prasanna et al., 2000).

Moored measurements at 18°N, 89.5°E during November 2009 to November 2010 showed frequent "jumps" in surface salinity (magnitude 0.2–1.2 psu) on time scales of 10 min to a few days (figure not shown). Based on observed surface currents and the Taylor hypothesis, Sengupta et al. (2016) deduced that the abrupt jumps are due to the passage of salinity-dominated density fronts with characteristic spatial scales of 1–40 km. Adams et al. (2019) analyzed high-resolution measurements using several shipborne and autonomous instruments simultaneously near to 10 km domain north of the WHOI mooring (18°N, 89.5°E), from 12 to 15 September 2015 (just prior to the deployment of our Seaglider around the mooring). Their measurements revealed prominent

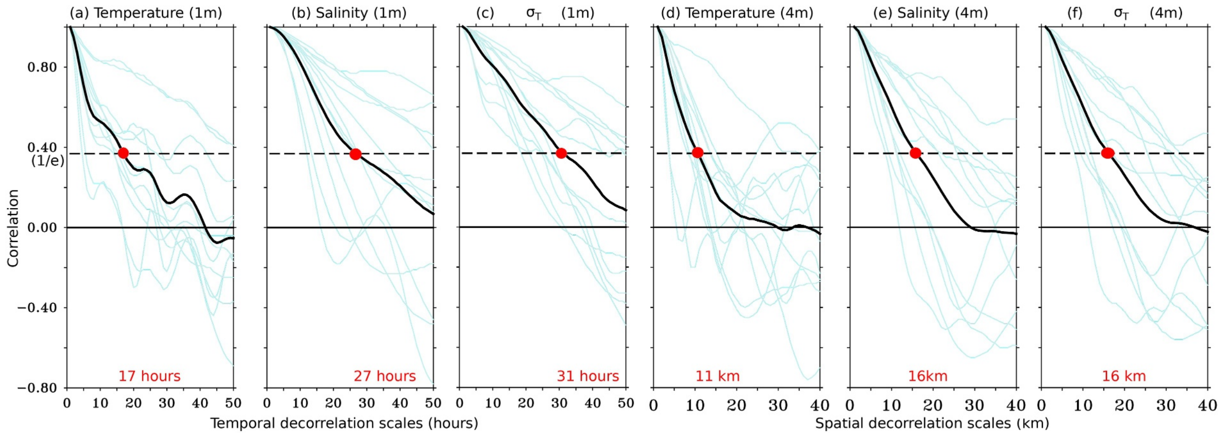

Figure 6. Temporal decorrelation scales (in hours) for (a) SST, (b) SSS, and (c) surface σ_t derived from the WHOI mooring during the period of individual SG15 butterfly patterns (light gray lines). Spatial decorrelation scales (in km) for (d) temperature, (e) salinity, and, (f) σ_t at 4 m derived from individual SG15 butterfly patterns (light gray lines). The thick black line in each panel represents the mean evolution of lagged correlation values. The thin horizontal line represents zero correlations, and the dashed horizontal line represents a correlation value of e^{-1} (i.e., 0.37). The red closed circle represents the mean of the spatial and temporal decorrelation values over all butterfly patterns.

lateral variability in salinity, temperature, vertical shear of ocean currents, mixed layer depth, and turbulent vertical fluxes in the ocean, at 1–10 km scale modulated by the semi-diurnal tide, diurnal cycle, and near-inertial oscillations. Although the effective resolution of our Seaglider observations is approximately 3 km, sub-mesoscale variations of salinity, temperature, and density are clearly present through the 3-month survey (Figure 6).

It is known that the nBoB is an active region of mesoscale dynamics (e.g., Chen et al., 2018; Gopalan et al., 2000; Gordon et al., 2017). Lateral stirring of riverine freshwater by the basin-scale circulation, mesoscale eddies, and directly wind-forced "Ekman" flow determines the large-scale evolution of sea surface salinity in the region (Chaudhuri et al., 2021; Gordon et al., 2017; Shroyer et al., 2020; Sree Lekha et al., 2018, 2020). At the same time, confluent flows and strain in the mesoscale eddy field, as well as stretching of fresh and salty filaments by individual eddies, tend to sharpen lateral salinity and density gradients (Lucas et al., 2016; Mahadevan et al., 2016; McKie et al., 2024; Paul et al., 2021). Subsequently, dynamical instabilities (McWilliams, 2016; Taylor & Thompson, 2023) generate a rich field of submesoscale motions in the upper ocean (Adams et al., 2019; MacKinnon et al., 2016; McKie et al., 2024; Ramachandran et al., 2018; Ramachandran & Tandon, 2020).

3.3. Time Evolution of Mixed Layer Salinity

During the survey period, the mixed layer salinity shows a progressively increasing trend from 30.8 psu to 32.6 psu, embedded with a couple of small amplitude high-frequency variability with a range of 0.2 psu (Figures 7a and 7b). However, the intense freshening event observed between late October and mid-November is distinct from other high-frequency salinity anomalies because of its longer persistence (∼15 days) and its large magnitude (∼2.4 psu; Figures 7a and 7b). Following this freshening phase, the salinity gradually recovered to its pre-freshening magnitude (from 30.4 psu to 32.2 psu) in the subsequent 10 days by late November (Figure 7b).

The relative contributions of freshwater flux, horizontal advection, and vertical processes to the mixed layer salinity tendency, particularly during the period of the intense freshening and salinification events in late October and November, are examined using the mixed layer salinity budget (Figures 7c and 7d). In general, the sum of the individual terms and observed rate of change of mixed layer salinity are in reasonable agreement (Figure 7c) and provide confidence to evaluate further the relative importance of various forcing mechanisms determining its mixed layer salinity variability during the SG15 survey period.

The mixed layer salinity tendency exhibits a significant freshening tendency during late October and early November (∼−0.3 psu day^{-1}) and a salinification tendency during mid-November (0.23 psu day^{-1}; Figure 7d). The local freshwater flux contribution is insignificant for the modulation of near-surface salinity during the study period, except during the intense precipitation events as apparent during early October and late October to mid-

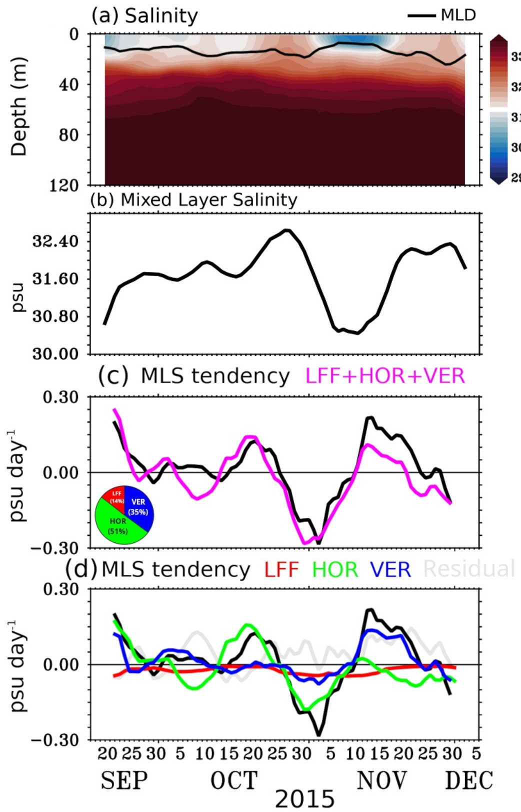

Figure 7. Temporal evolution of (a) depth-time section of salinity (psu), (b) ML averaged salinity (psu), (c) rate of change of ML salinity (black; psu day^{-1}) and the sum of local freshwater flux, horizontal advection and vertical processes (pink; psu day^{-1}) and (d) ML salinity tendency (black; psu day^{-1}), local freshwater flux (LFF; red; psu day^{-1}), horizontal advection (HOR; green; psu day^{-1}), vertical processes (VER; blue; psu day^{-1}) and residual (light gray; psu day^{-1}) derived from the SG15 survey track during the period from 17 September to 06 December 2015. In panel (a), the thick line represents MLD (m), and the thin line represents ILD (m). The difference between MLD and ILD is the BL thickness. In panel (c), the inset pie chart shows the percentage contributions (marked as a number in individual slice) of net surface heat flux (red; 14%), horizontal advection (green; 51%), and vertical processes (blue; 35%) to the sum of the mixed layer salinity budget forcing terms, and it is estimated as the ratio of the absolute value of each term to the sum of the absolute values of all three terms. A 10-day smoothing is applied to the budget terms, and a 7-day smoothing for other panels for better readability.

November (Figures 4g and 7d). The local freshwater flux due to precipitation events contributes (−0.03 psu day^{-1}) to the mixed layer freshening event in October, while it counteracts (−0.05 psu day^{-1}) the salinification tendency during mid-November.

With the presence of low-salinity water overlying the subsurface high-salinity water, mixed layer entrainment generally facilitates the salinification of the mixed layer in the BoB (Girishkumar et al., 2014; Pant et al., 2015; Wilson & Riser, 2016). The role of entrainment in determining the mixed layer salinity variability through salinification of the mixed layer was insignificant throughout the survey period, except during the increasing phase of mixed layer salinity tendency in mid-November (Figure 7d). During this phase, the entrainment term acts as the predominant term in determining mixed layer salinity tendency. Note that during the intense freshening phase of the mixed layer in early November, the entrainment term shows a negligible contribution (−0.08 psu day^{-1}), which might be attributed to the suppression of entrainment due to the re-stratification of the mixed layer (Figures 7a and 7d).

Compared to local freshwater flux and entrainment processes, the overall mixed layer salinity tendency during the study period is primarily determined by horizontal advection (Figure 7d). These characteristics are apparent as a strong temporal correspondence between horizontal advection and the mixed layer salinity tendency except during 11–28 November 2015, where horizontal advection showed a freshening tendency in contrast with the salting tendency by mixed layer salinity tendency (0.2 psu day^{-1}). However, the entrainment term provides a reasonable contribution to the mixed layer salinity tendency during this period (0.15 psu day^{-1}). Thus, the horizontal advection came out as the dominant factor in determining the mixed layer freshening in early November (−0.18 psu day^{-1}), and it acted as a secondary contributing factor during the salinification phase in mid-November (−0.07 psu day^{-1}), while entrainment plays a primary role. In summary, local freshwater flux, horizontal advection and vertical processes contribute approximately 14%, 51%, and 35%, respectively, to determine the sum of all forcing terms in the salinity budget equation (Figure 7c; inset pie-diagram).

The mixed-layer salinity budget analysis presented in this study considers the same study region in the northern BoB, with a study period that partially overlaps with that examined by Thangaprakash et al. (2025). However, an important distinction between the two studies lies in the spatial resolution of the data sets used to estimate the horizontal salinity gradients for the horizontal advection term. In Thangaprakash et al. (2025), the horizontal gradients of sea surface salinity were estimated using observations from three moorings separated by distances of approximately 30 km. In contrast, the present study estimates the horizontal salinity gradient using mixed-layer-averaged salinity derived from high-resolution glider observations, with an effective spatial resolution of ∼8 km. The higher spatial resolution of the glider-based data set allows for a better representation of the lateral salinity gradients associated with small-scale freshwater features in the northern BoB. Despite these differences in data sets and spatial scales, the conclusions drawn from the present analysis remain consistent with earlier studies of mixed-layer salinity variability in the BoB (Buckley et al., 2020; Chaitanya et al., 2021; Parampil et al., 2010; Thangaprakash et al., 2025), which highlight that the near-surface salinity variability is predominantly controlled by horizontal advection, while vertical entrainment plays a secondary role.

3.4. Evolution of Barrier Layer Temperature and Inversion

Consistent with previous observational studies over the BoB (Girishkumar, Ravichandran, & Han, 2013; Girishkumar, Ravichandran, & McPhaden, 2013; Thadathil et al., 2016), the barrier layer thickness and magnitude of

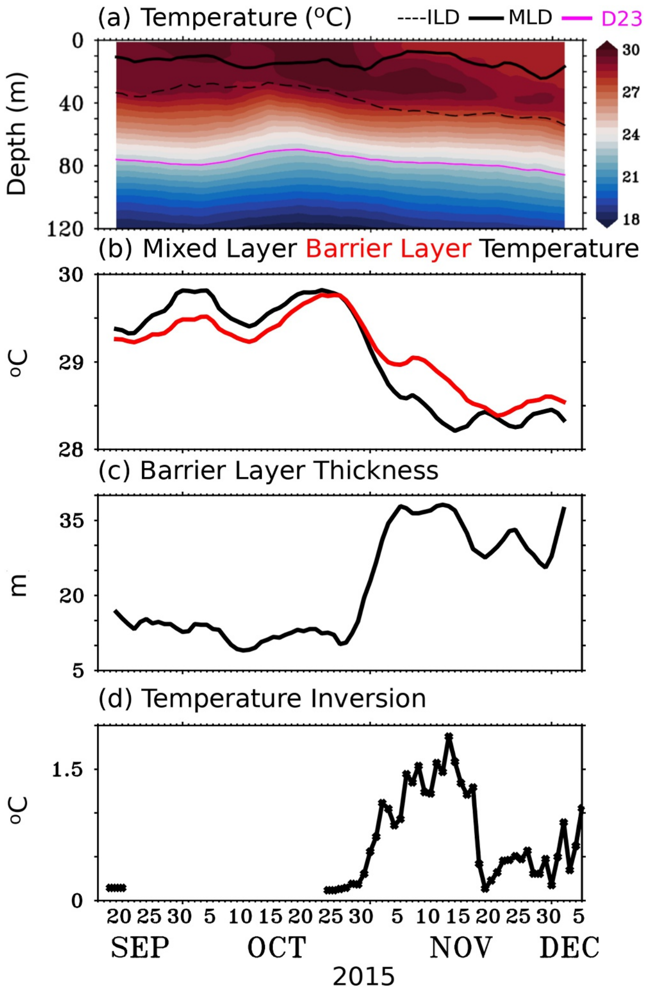

Figure 8. Temporal evolution of (a) depth-time section of temperature (°C), (b) ML averaged temperature (°C), (c) BL thickness (m), (d) the magnitude of temperature inversion (°C) derived from the SG15 survey track during the period from 17 September to 06 December 2015. In panel (a), the thick line represents MLD (m), and the thin line represents ILD (m). The difference between MLD and ILD is the BL thickness. A 7-day smoothing is applied to all panels for better readability.

temperature inversion during the SG15 survey show strong temporal correspondence, with stronger inversions coinciding with a thicker barrier layer (Figures 8a, 8c, and 8d). During the first half of the survey period, the barrier layer is thin (<15 m), and the occurrence of temperature inversion is roughly absent (Figures 8a, 8c, and 8d). However, during the second half of the SG15 survey, the magnitude of the temperature inversion remains high, reaching 2°C, in conjunction with a thick barrier layer (35–40 m; Figures 8c and 8d). Moreover, we find a strong temporal correspondence with increasing barrier layer thickness and the magnitude of temperature inversion during late October 2015 and early November 2015. Although the BL remains relatively thick (>25 m) until November 30, 2015, the magnitude of temperature inversion peaks (∼1.5°C) around 15 November subsequently falls to more than half of its strength (∼0.5°C) between 20 November and 30 November 2015 (Figures 8c and 8d).

During the first half of the survey period, the MLD and ILD were centered around 10 and 28 m, respectively, showing not much variability compared to the later part of the survey (Figure 8a). Consequently, the modulation of barrier layer (BL) thickness was small, with values centered around 15 m (Figure 8c). In contrast, during the second half of the survey, the BL exhibited sudden increases due to the divergence of ILD and MLD, resulting from the combined effect of MLD shoaling and ILD deepening (Figure 8a). The shoaling of the MLD during this period is primarily attributed to the presence of low-salinity water in the near-surface layer. Our mixed layer salinity budget analysis indicates that these freshenings in the near-surface layer are due to the combined effect of horizontal advection and local freshwater flux (Figure 7d; red and green lines). Both westward propagating meso-scale features and local ekman pumping velocity can contribute to the deepening of ILD. Satellite sea surface height anomaly (SSHA) shows a westward propagating downwelling mesoscale eddy with positive SSHA; at the same time, Ekman pumping velocity estimated from satellite winds indicates downwelling. This suggests that both these features are favorable for the deepening of ILD (Figures 8 and 9; Girishkumar, Ravichandran, & Han, 2013; Yu, 2003). The temporal evolution of SSHA and Ekman pumping velocity during the survey period in 2015 in the nBoB is consistent with climatological conditions (Figure 9). However, the magnitude of the rate of change of ILD and Ekman pumping velocity indicates that the relatively smaller contribution from the latter parameters on the former (Figure 9e). These characteristics suggest that the westward propagating downwelling Rossby wave, as reflected in the positive SSHA values in the hovmoller diagram, determines the deepening of ILD during the second half of the survey. Moreover, the statistical comparison between MLD and ILD with respect to barrier layer thickness reveals a strong positive correlation (0.9; positive correlation indicates deepening of ILD increases barrier layer thickness) between ILD and barrier layer thickness, whereas MLD exhibits a moderate negative correlation (−0.5; negative correlation indicates shallowing of MLD increase barrier layer thickness). These characteristics suggest that ILD plays a greater role than MLD in determining the magnitude of barrier layer thickness (Figure 9).

The mixed layer temperature is slightly higher than barrier layer temperature during the first half of the survey period, where the BL thickness and temperature inversion are thin or nearly absent. During the second half of the survey period, the mixed layer temperature is slightly lower than barrier layer temperature, where the BL thickness and temperature inversion are thick and strong (Figure 8b).

3.5. Barrier Layer and Mixed Layer Temperature Budgets

In the presence of a barrier layer with strong near-surface salinity stratification, cooling of the mixed layer relative to the barrier layer or warming the barrier layer relative to the mixed layer is conducive to the formation of

10.1029/2025JC023682

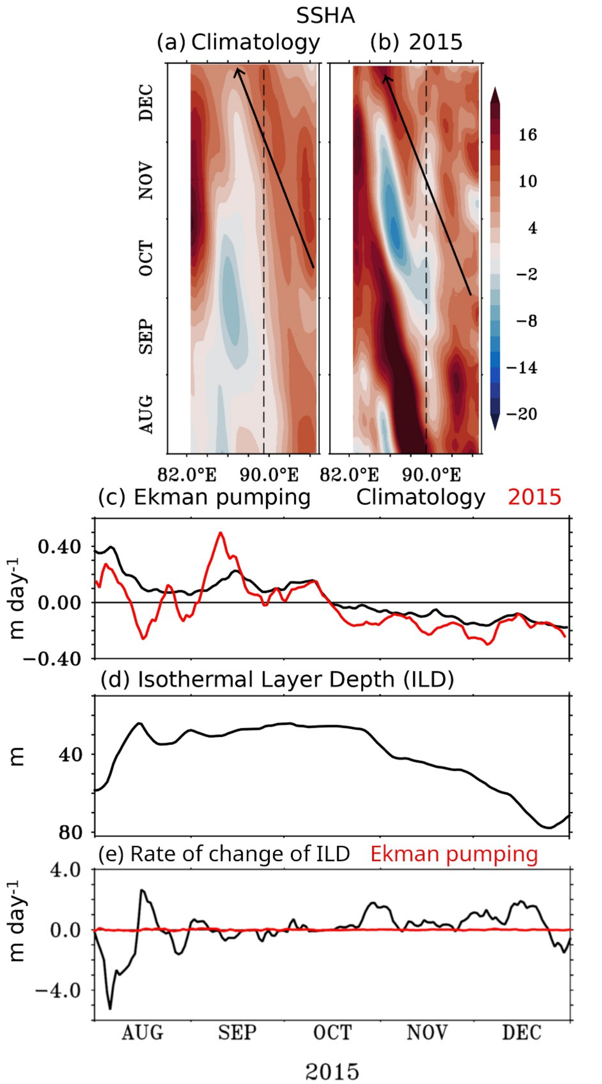

Figure 9. Hovmöller diagram showing the evolution of sea surface height anomalies (cm) averaged over the latitudinal band 17°N–19°N in the BoB for (a) climatology (1993–2024) and (b) for the year 2015. (c) Temporal evolution of Ekman pumping velocity (m day^{-1}) averaged over the region 17°N–19°N, 89°E–90°E for climatology (2015–2024, black line) and for the year 2015 (red line), (d) Isothermal Layer Depth (ILD; m) and (e) rate of change of ILD (black) and ekman pumping (red; m day^{-1}). The black arrow line in panels (a, b) represents the westward propagating mesoscale features.

temperature inversion (Girishkumar, Ravichandran, & Han, 2013; Kurian & Vinayachandran, 2006; Thadathil et al., 2016). In this section, we examine and compare individual terms in the barrier layer temperature budget with corresponding terms in the mixed layer temperature budget to understand the origin and time evolution of temperature inversion during the glider survey period (Figures 10–12). The sum of the effective heat flux (i.e., divergence of shortwave radiation) in the mixed layer ($Q_{\mathrm{EF\_ML}}$), horizontal advection, and entrainment terms agrees reasonably well with the mixed layer temperature tendencies (Figures 10a and 11a). Similarly, the sum of the effective heat flux (i.e., divergence of shortwave radiation) in the barrier layer ($\mathrm{Q_{EF\_BL}}$), barrier layer horizontal advection, and barrier layer vertical processes shows a good temporal correspondence with the barrier layer temperature tendencies. Please note that, the summed contribution of the forcing terms in the barrier-layer temperature budget equation has the opposite sign to the barrier-layer temperature tendency during the development of the temperature inversion, such as, specifically, the sum of the forcing terms in the barrier layer budget equation indicates a weak warming tendency, whereas the barrier-layer temperature tendency shows weak cooling. These characteristics provide confidence in using barrier layer temperature budget terms in conjunction with mixed layer temperature budget terms to investigate the relative importance of the factors that modulate the magnitude of temperature inversion.

Thadathil et al. (2016) and Thangaprakash et al. (2016) performed a mixed layer temperature budget analysis in the BoB using observations from the RAMA mooring array in the central and southern BoB at 8°N, 90°E; 12°N, 90°E; and 15°N, 90°E. However, the present study focuses on the northern BoB (~18°N, 90°E), where the freshwater stratification is considerably stronger than in the central and southern regions of the basin. Thadathil et al. (2016) used a mixed layer temperature budget to examine the factors that modulate the magnitude of temperature inversion in the BoB. However, in the present study, we extend their work by comparing the different terms in the mixed layer and barrier layer temperature budgets and by assessing the relative contributions of surface heat flux, horizontal advection, and vertical processes in modulating temperature inversion within the barrier layer.

3.5.1. Mixed Layer Temperature Budget

The rate of change in mixed layer temperature shows mild warming (~0.05°C day^{-1}) and cooling (~−0.05°C day^{-1}) tendencies during the first half and strong cooling tendency (~−0.15°C day^{-1}) during the second half of the SG15 survey period (Figure 10). The $Q_{\mathrm{EF\text{-}ML}}$ was positive (~0.2°C day^{-1}) in the first part of the survey but became negative (~−0.25°C day^{-1}) in the second half (Figure 10b; red line). The vertical processes provide a relatively minor contribution to the mixed layer temperature variability as compared to $Q_{\mathrm{EF\text{-}ML}}$ except during late-October and mid-November. One noticeable difference in the vertical processes term is that it shows a mild cooling tendency (~−0.05°C day^{-1}) during the first phase of the survey period compared to a warming tendency (~0.15°C day^{-1}) in the latter phase; these differences can be attributed to the absence and presence of temperature inversion (Figures 8 and 10). The magnitude of horizontal advection terms is comparable to that of vertical terms, and their evolution is characterized by alternating positive and negative tendencies (±0.075°C day^{-1}). Overall, the analysis shows that $Q_{\mathrm{EF\text{-}ML}}$ is the major factor influencing mixed layer temperature variability during the SG15 survey. In summary, effective heat flux in the mixed layer, horizontal advection and vertical processes contribute approximately 43%, 35%, and 22%, respectively, to determine the sum of forcing terms in the mixed layer temperature budget equation (Figure 10a; inset pie-diagram).

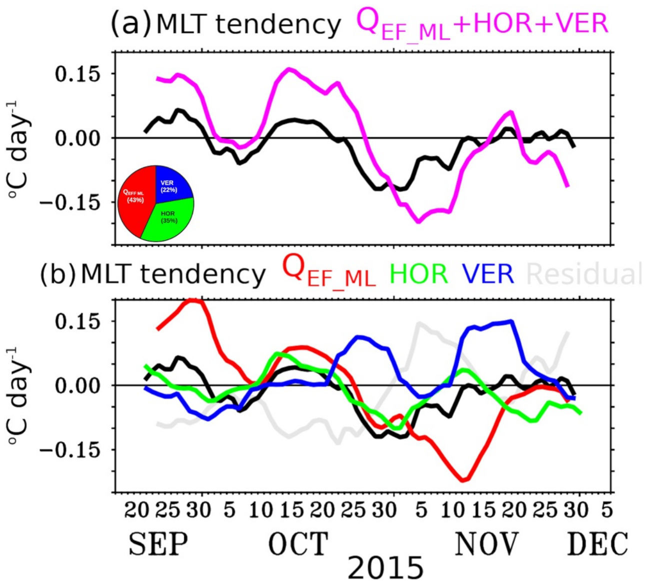

Figure 10. The different terms in the ML temperature budget terms during the period from 17 September to 6 December 2015. (a) Rate of change of ML temperature (black; °C day^{-1}) and the sum of $Q_{\mathrm{EF\_ML}}$, horizontal advection, and vertical processes (pink; °C day^{-1}) and (b) mixed layer temperature tendency (black; psu day^{-1}), $Q_{\mathrm{EF\_ML}}$ (red; °C day^{-1}), horizontal advection (green; °C day^{-1}), vertical processes (blue; °C day^{-1}), and residual (light gray; °C day^{-1}). In panel (a), the inset pie chart shows the percentage contributions (marked as a number in individual slice) of net surface heat flux (red; 43%), horizontal advection (green; 35%), and vertical processes (blue; 22%) to the sum of the mixed layer temperature budget forcing terms, and it is estimated as the ratio of the absolute value of each term to the sum of the absolute values of all three terms. A 10-day running mean is applied to the budget terms for better readability.

3.5.2. Barrier Layer Temperature Budget

The rate of change in barrier layer temperature shows mild warming (~0.05°C day^{-1}) and cooling (~−0.03°C day^{-1}) tendencies during the first phase and shows a strong cooling tendency (~−0.1°C day^{-1}) during the second phase of the SG15 survey (Figure 11). Our analysis shows that both mixed layer and barrier layer temperature tendencies exhibited nearly comparable magnitudes, with mild variability observed during the second half of the survey period, when freshwater stratification and temperature inversion were present. The standard deviations were 0.17°C day^{-1} and 0.15°C day^{-1} for the mixed layer and barrier layer, respectively (Figure 11). Compared to the individual terms on the right-hand side of the mixed layer temperature budget equation, the terms in the barrier layer budget showed relatively weaker temporal variability throughout the survey period. The standard deviation of effective surface heat flux (0.2°C day^{-1}), horizontal advection (0.1°C day^{-1}) and vertical processes (0.2°C day^{-1}) of mixed layer temperature budget terms are higher than the corresponding terms in the barrier layer temperature budget, which are 0.01°C day^{-1}, 0.1°C day^{-1}, and 0.02°C day^{-1}, respectively. The term $Q_{\mathrm{EF\text{-}BL}}$ is positive (~0.03°C day^{-1}) throughout the observation period without substantial temporal variability (Figure 11; red line). Horizontal advection is positive throughout the survey, except during early October and November 2015. Vertical processes play an important role in determining the barrier layer temperature in the first part of the survey except mid-October, as can be seen from the temporal coherence between these two terms until the first week of November (Figure 11; cf. black and blue lines). In summary, effective heat flux in the barrier layer, horizontal advection and vertical processes contribute approximately 16%, 31%, and 53% respectively, to determine the sum of all forcing terms in the barrier layer temperature budget equation (Figure 11a; inset pie-diagram).

3.5.3. Comparison Between Barrier Layer and Mixed Layer Temperature Budget Terms

During the first phase of the survey period, with a weak temperature inversion, the warming of the mixed layer (0.2°C day^{-1}) due to the effective heat flux is much higher than that of the barrier layer (0.03°C day^{-1}; Figure 12a). However, in the second phase, the effective heat flux exhibits a predominant cooling tendency in the mixed layer (−0.23°C day^{-1}), contrasting with a mild warming tendency in the barrier layer (0.03°C day^{-1}). As noted earlier, this is conducive to the formation of temperature inversion.

The contribution of horizontal advection has comparable magnitudes in the mixed-layer and barrier-layer temperature budgets throughout the survey period, with notable differences during 18 October–07 November 2015 and 16–27 November 2015. During these two periods, horizontal advection tends to cool the mixed layer (−0.1°C day^{-1}), while it tends to warm the barrier layer (Figure 12b), thus favoring the growth of temperature inversions.

For the majority of the survey period, vertical processes inhibited the formation of temperature inversion. In particular, the barrier layer exhibited either more cooling or less warming than the mixed layer due to vertical processes (Figure 12c). For example, during 21 October–04 November and 10–23 November 2015, the mixed layer warmed at a higher rate (0.12–0.15°C day^{-1}) than the barrier layer (0.05°C day^{-1}), which inhibited the formation of temperature inversion (TI). Consequently, the vertical process term cooled the mixed layer more than the barrier layer during a short time period in early October and early November, which only favors the development of TI.

The combined effect of heat flux, lateral advection, and vertical processes contributes to higher warming rates in the mixed layer than in the barrier layer during the initial phase, and there is no temperature inversion until 25 October (Figures 8 and 12d). In contrast, the second half of the survey is characterized by a significant temperature inversion. During this period, the sum of the terms on the right-hand side of the mixed layer and barrier

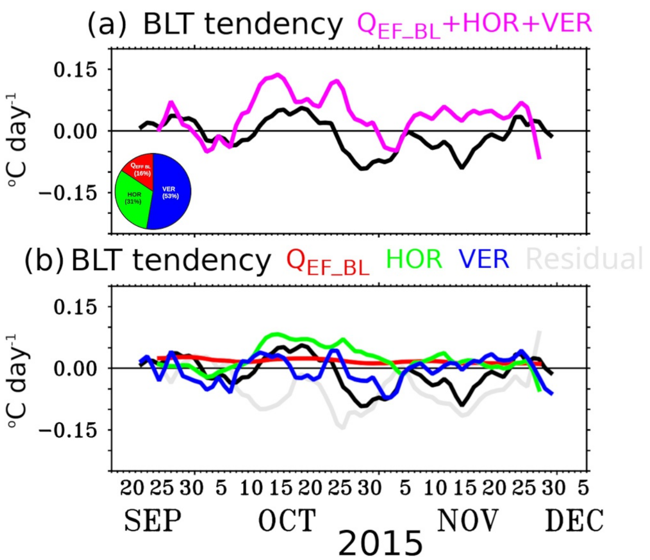

Figure 11. As in Figure 10, but for the BL temperature budget. All units are in °C day^{-1}. In panel a, the inset pie chart shows the percentage contributions (marked as a number in individual slice) of net surface heat flux (red; 16%), horizontal advection (green; 31%), and vertical processes (blue; 53%) to the sum of the barrier layer temperature budget forcing terms, and it is estimated as the ratio of the absolute value of each term to the sum of the absolute values of all three terms.

layer temperature budget equations indicates a cooling of the mixed layer (−0.2°C day^{-1}) compared to mild warming (0.05°C day^{-1}) in the barrier layer (Figure 12d; compare black and red lines) leading to strong temperature inversion.

The pronounced cooling of the mixed layer by 1.5°C in the 2 weeks by the end of October to mid-November coincides with an increase in barrier layer thickness from 10 m to nearly 40 m (Figure 8). A temperature inversion first appears in the last week of October, and its strength grows to nearly 1.5°C by mid-November (see Figure 8c). As noted earlier, the temperature inversion is primarily driven by the difference in effective heat flux between the base of the mixed layer and the base of the isothermal layer, with a secondary contribution from horizontal advection (Figure 12). During the initial phase of the second half of the survey, the sum of all terms on the right-hand side of the barrier layer temperature budget shows a higher warming rate than the mixed layer temperature budget terms, leading to a stronger temperature inversion. However, as these differences reduce (0.08°C day^{-1}) in the latter phase of the second half of the survey, the magnitude of the temperature inversion correspondingly decreases (0.5°C). Though ILD was increasing during this period, the barrier layer thickness reduced to 25–30 m due to the slight deepening of the mixed layer. Thus, the magnitude of the temperature inversion decreased during the latter phase of the second half of the survey period. During the initial phase of the survey, the sum of all terms on the right-hand side of the mixed layer temperature budget indicates a comparable or slightly higher warming rate than that of the barrier layer, leading to a weak temperature inversion.

4. Summary and Conclusion

The near-surface hydrographic state in the nBoB plays a crucial role in determining many aspects of the weather and climate of the Indian subcontinent. Hence, it is imperative to understand the factors that modulate the near-surface hydrographic state and its variability in the nBoB.

To advance our understanding of near-surface hydrographic features in the nBoB, a Seaglider equipped with temperature, conductivity, and biogeochemical sensors was deployed in the nBoB for a mission mode from 17 September to 6 December 2015 (SG15). During its mission, SG15 performed 12 repeated butterfly patterns spanning approximately 22 km zonally and meridionally around the WHOI mooring at 18.01°N, 89.46°E. The glider survey period between September and December coincides with key climatological hydrographic features in the nBoB, such as the appearance and growth of barrier layer thickness and temperature inversion, starting from a minimum in October to its maximum in February. In addition, the study period also coincides with the existence of a large magnitude of lateral salinity gradient at the survey site.

In this study, we use unprecedented concurrent measurements of the vertical profiles of temperature and salinity from the glider, as well as near-surface meteorological parameters, near-and sub-surface oceanographic parameters and current velocities from moorings to understand the temporal and spatial decorrelation length scales of SSS and SST, and the physical factors that determine the time evolution of temperature inversion using the temperature budget of the mixed layer and barrier layer.

The horizontal distribution of near-surface glider observations exhibits the dominance of sub-mesoscale filaments, which are distinguished by substantial horizontal density gradients caused primarily by lateral salinity variations on characteristics spatial scales of around 15 km and temporal scales of around 30 hr. Analysis using the Turner angle (Tu_H) corroborates that lateral variation of salinity is the main determinant of horizontal density gradients in the mixed layer. We also found that the horizontal gradient of salinity is significantly reduced below the mixed layer, while temperature gradients increasingly dominate density variability, consistent with previous multi-platform observations in the same region of the BoB (Adams et al., 2019).

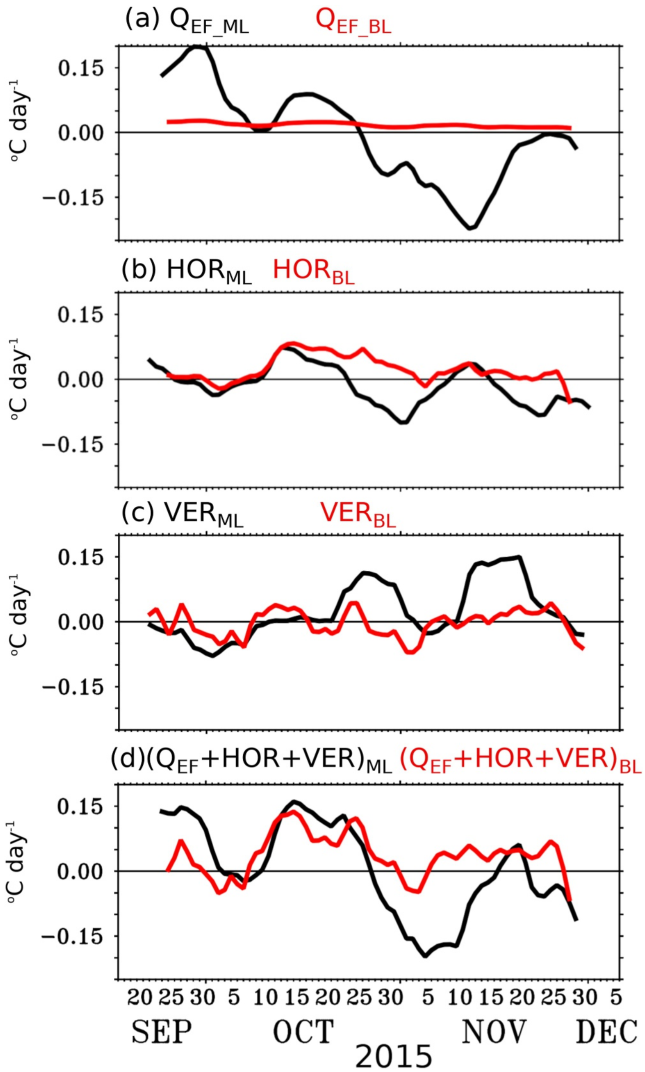

Figure 12. Comparison between the different terms in the ML temperature budget (black) and BL temperature budget (red), (a) $Q_{EF,}$ (b) horizontal advection, (c) vertical processes, and (d) sum of Q_{EF}, horizontal advection, and vertical processes. All units are in °C day^{-1}. A 10-day running mean is applied to the budget terms for better readability.

Consistent with previous studies over the nBoB, we calculated a salinity budget of the mixed layer, which shows that near-surface salinity variability is primarily determined by horizontal advection in the presence of substantial lateral salinity gradients. However, the influence of horizontal advection can be either enhanced or suppressed using entrainment processes and local freshwater fluxes resulting from precipitation events.

During the initial part of the survey period (17 September to 26 October 2015), the BL is thin (<20 m), and temperature inversion is weak (<0.1°C) and sporadic. However, the magnitude of the temperature inversion remained persistently high, reaching nearly 1.5°C, in conjunction with a significant BL thickness (30–40 m) during the second part (27 October to 6 December 2015) of the survey. We find that the pronounced cooling of the mixed layer compared to the barrier layer, primarily driven by differential heating of the mixed layer and BL due to effective heat flux, and secondarily by horizontal advection, plays a crucial role in the formation of temperature inversion. On the other hand, the combined contributions of all terms in the temperature budget indicate a slightly higher warming rate in the mixed layer compared to the barrier layer, leading to a weak temperature inversion during the first phase of the survey.

Though combined measurements from the glider and moorings provide new insights into the various factors that cause the variability of the mixed layer salinity and temperature and barrier layer temperature, this study has certain limitations. For instance, using three-day high-resolution measurements from shipborne and autonomous instruments collected close to our study region near the WHOI mooring just before our study period (12–15 September 2015), Adam et al. (2019) showed the small-scale lateral variability of the temperature, salinity, and MLD in the ocean at the order of 1–10 km scale. Please note that the effective resolution of the glider observations is approximately 3 km in space and 5 hr in time. Hence, the present study cannot resolve variability associated with submesoscale processes shorter than these time and spatial scales.

Another possible source of error could be the choice of criteria used for estimating MLD. In this study, we have used variable density criterion of 0.125 kg m^{-3} and the same was compared with 0.1 kg m^{-3} and 0.2 kg m^{-3}. The RMSD is found to be 1.8 and 4.6 m, respectively, with a correlation of 0.9 for both. Also, our budget is not sensitively significant to the choice of MLD. We performed the budget using 0.2 kg m^{-3} variable density criterion and found that the RMSD of 10-day smoothed terms of mixed layer heat budget terms with respect to our choice is smaller than its variability. Further, biases due to the sensor drifts, sensor electronics and calibration errors could also be added to the limitations.

Overall, our study provides quantitative insights into the small-scale processes controlling mixed layer and barrier layer temperature evolution in the northern BoB. The near-surface glider and mooring observations reveal a dominance of sub-mesoscale features characterized by strong horizontal density gradients driven primarily by lateral salinity variations, with spatial scales of ∼15 km and temporal scales of ∼30 hr. These sub-mesoscale features are typically unresolved in most ocean models, suggesting that their effects on modulation of near-surface temperature and salinity may be under-represented and it can act as a probable source of error in the simulation of oceanic hydrographic state over the northern BoB in the ocean models. Moreover, we also find that the magnitude of temperature inversion is determined by differential heating of the mixed layer and barrier layer through combined effects of the one-dimensional processes such as atmospheric heat flux and three dimensional processes such as horizontal advection. Considering the importance of temperature inversion on the modulation of mixed layer temperature evolution, our present study underpins the need to accurately represent the three dimensional processes to appropriately represent the magnitude of temperature inversion in the ocean general circulation models. The results from this study will be helpful for the ocean modeling community to optimize the model resources particularly on the existence of small spatial and high temporal scale patterns. In addition, the present study also underpins the need for the accurate simulation of three-dimensional oceanic parameters and better representation of penetrative shortwave radiation and atmospheric fluxes to accurately reproduce the evolution of the mixed layer and barrier layer temperature in the BoB.

Conflict of Interest

The authors declare no conflicts of interest relevant to this study.

Availability Statement

SMAP salinity data are produced by Remote Sensing Systems and sponsored by the NASA Ocean Salinity Science Team. Data are available at www.remss.com. Argo gridded products are available on the INCOIS LAS server (https://las.incois.gov.in/), and data can be downloaded from the tab "Gridded Product based on Variational Analysis Methodology" under "Argo Data Products." The Seaglider data is available from https://doi.org/10.5281/zenodo.19204101 and OMNI mooring data sets are available from https://incois.gov.in/site/datainfo/moored_omnidata_stock.jsp?parameter=999999&buoy=BD08. The mooring data used in this study are quality-controlled and distributed by WHOI, and data are available at https://uop.whoi.edu/projects/Bengal/QCData.html. The altimeter (SLA) products are distributed by E.U. Copernicus Marine Service Information (CMEMS) (Global Ocean Gridded L4 Sea Surface Heights And Derived Variables Reprocessed 1993 Ongoing, 2024). The merged daily SSHA data is distributed by the Copernicus-GlobColour, and the data is available at http://marine.copernicus.eu.

Acknowledgments

The encouragement provided by the Director, INCOIS, is gratefully acknowledged. The Seaglider is procured as part of the Ministry of Earth Sciences (MoES) funded Monsoon Mission project, "Coupled Physical Processes in the BoB and Monsoon Air-Sea Interaction (Ocean Mixing and Monsoon; OMM)." This work was carried out as part of V. P. Thangaprakash, Ph.D. work. The deployment and recovery of Seaglider were carried out from the ORV Sagar Nidhi and ORV Sagar Manjusha, respectively. The WHOI mooring was deployed from ORV Sagar Nidhi, and the recovery was from ORV Sagar Kanya. We thank the captain, crew, and vessel management cell of NIOT and NCPOR for their support. This is INCOIS contribution 719.

References

Adams, K., MacKinnon, J., Lucas, A. J., Nash, J., Shroyer, E., & Farrar, J. T. (2019). Multi-platform observations of small-scale lateral mixed layer variability in the northern Bay of Bengal. *Deep Sea Research Part II: Topical Studies in Oceanography*, *168*(2019), 104629. https://doi.org/10.1016/j.dsr2.2019.07.017

Akhil, V. P., Durand, F., Lengaigne, M., Vialard, J., Keerthi, M. G., Gopalakrishna, V. V., et al. (2014). A modeling study of the processes of the surface salinity seasonal cycle in the Bay of Bengal. *Journal of Geophysical Research: Oceans*, *119*(6), 3926–3947. https://doi.org/10.1002/2013jc009632

Ashin, K., Girishkumar, M. S., Suprit, K., & Thangaprakash, V. P. (2019). Observed upper ocean seasonal and intraseasonal variability in the Andaman Sea. *Journal of Geophysical Research: Oceans*, *124*(10), 6760–6786. https://doi.org/10.1029/2019JC014938

Balaguru, K., Taraphdar, S., Leung, L. R., & Foltz, G. R. (2014). Increase in the intensity of postmonsoon Bay of Bengal tropical cyclones. *Geophysical Research Letters*, *41*(10), 3594–3601. https://doi.org/10.1002/2014GL060197

Bentamy, A., Grodsky, S. A., Carton, J. A., Croizé-Fillon, D., & Chapron, B. (2012). Matching ASCAT and QuikSCAT winds [Dataset]. *Journal of Geophysical Research*, *117*(C2), C02011. https://doi.org/10.1029/2011JC007479

Buckley, J. M., Mingels, B., & Tandon, A. (2020). The impact of lateral advection on SST and SSS in the northern Bay of Bengal during 2015. *Deep Sea Research Part II: Topical Studies in Oceanography*, *172*, 104653. https://doi.org/10.1016/j.dsr2.2019.104653

Chaitanya, A. V. S., Vialard, J., Lengaigne, M., d'Ovidio, F., Riotte, J., Papa, F., & James, R. A. (2021). Redistribution of riverine and rainfall freshwater by the Bay of Bengal circulation. *Ocean Dynamics*, *71*(11–12), 1113–1139. https://doi.org/10.1007/s10236-021-01486-5

Chaudhuri, D., Sengupta, D., D'Asaro, E., & Shivaprasad, S. (2021). Trapping of wind momentum in a salinity-stratified ocean. *Journal of Geophysical Research: Oceans*, *126*(12), e2021JC017770. https://doi.org/10.1029/2021JC017770

Chaudhuri, D., Sengupta, D., D'Asaro, E., Venkatesan, R., & Ravichandran, M. (2019). Response of the salinity-stratified Bay of Bengal to cyclone phailin. *Journal of Physical Oceanography*, *49*(5), 1121–1140. https://doi.org/10.1175/JPO-D-18-0051.1

Chelton, D. B., de Szoeke, R. A., Schlax, M. G., El Naggar, K., & Siwertz, N. (1998). Geographical variability of the first baroclinic Rossby radius of deformation. *Journal of Physical Oceanography*, *28*, 433–460. https://doi.org/10.1175/1520-0485(1998)028<0433>2.0.CO;2

Chen, G., Li, Y., Xie, Q., & Wang, D. (2018). Origins of eddy kinetic energy in the Bay of Bengal. *Journal of Geophysical Research: Oceans*, *123*(3), 2097–2115. https://doi.org/10.1002/2017JC013455

Chowdhury, M. R., & Ward, N. (2004). Hydro-meteorological variability in the greater Ganges–Brahmaputra–Meghna basins. *International Journal of Climatology*, *24*(12), 1495–1508. https://doi.org/10.1002/joc.1076

Cole, S. T., Rudnick, D. L., & Colosi, J. A. (2010). Seasonal evolution of upper-ocean horizontal structure and the remnant mixed layer. *Journal of Geophysical Research*, *115*(C4), C04012. https://doi.org/10.1029/2009JC005654

Dai, A., Qian, T., Trenberth, K. E., & Milliman, J. D. (2009). Changes in continental freshwater discharge from 1948 to 2004. *Journal of Climate*, *22*(10), 2773–2792. https://doi.org/10.1175/2008jcli2592.1

De Boyer Montégut, C., Mignot, J., Lazar, A., & Cravatte, S. (2007). Control of salinity on the mixed layer depth in the world ocean: 1. General description. *Journal of Geophysical Research*, *112*(C6), C06011. https://doi.org/10.1029/2006JC003953

Fairall, C. W., Bradley, E. F., Hare, J. E., Grachev, A. A., & Edson, J. B. (2003). Bulk parameterization of air-sea fluxes: Updates and verification for the COARE algorithm [Software]. *Journal of Climate*, *16*(4), 571–591. https://doi.org/10.1175/1520-0442(2003)016<0571:BPOASF>2.0.CO;2

Girishkumar, M. S., Joseph, J., McPhaden, M. J., & Pattabhi Ram Rao, E. (2021). Atmospheric cold pools and their influence on sea surface temperature in the Bay of Bengal. *Journal of Geophysical Research: Oceans*, *126*(9), e2021JC017297. https://doi.org/10.1029/2021JC017297

Girishkumar, M. S., Joseph, J., Thangaprakash, V. P., Pottapinjara, V., & McPhaden, M. J. (2017). Mixed layer temperature budget for the northward propagating Summer Monsoon Intraseasonal Oscillation (MISO) in the Central Bay of Bengal. *Journal of Geophysical Research: Oceans*, *122*(11), 8841–8854. https://doi.org/10.1002/2017JC013073

Girishkumar, M. S., Ravichandran, M., & Han, W. (2013). Observed intraseasonal thermocline variability in the Bay of Bengal. *Journal of Geophysical Research: Oceans*, *118*(7), 3336–3349. https://doi.org/10.1002/jgrc.20245

Girishkumar, M. S., Ravichandran, M., & McPhaden, M. J. (2013). Temperature influence and their influence on the mixed layer heat budget during the winters of 2006–2007 and 2007–2008 in the Bay of Bengal. *Journal of Geophysical Research: Oceans*, *118*(5), 2426–2437. https://doi.org/10.1002/jgrc.20192

Girishkumar, M. S., Ravichandran, M., McPhaden, M. J., & Rao, R. R. (2011). Intraseasonal variability in barrier layer thickness in the south central BoB. *Journal of Geophysical Research*, *116*(C3), C03009. https://doi.org/10.1029/2010JC006657

Girishkumar, M. S., Suprit, K., Chiranjivi, J., Udaya Bhaskar, T. V. S., Ravichandran, M., Venkat Shesu, R., & Pattabhi Rama Rao, E. (2014). Observed oceanic response to tropical cyclone *Jal* from a moored buoy in the south-western Bay of Bengal. *Ocean Dynamics*, *64*(3), 325–335. https://doi.org/10.1007/s10236-014-0689-6

Global Ocean Gridded L4 Sea Surface Heights And Derived Variables Reprocessed 1993 Ongoing. (2024). E.U. Copernicus Marine Service Information (CMEMS) [Dataset]. *Marine Data Store (MDS)*. https://doi.org/10.48670/moi-00148

Gomes, H. R., Goes, J. I., & Saino, T. (2000). Influence of physical processes and freshwater discharge on the seasonality of phytoplankton regime in the BoB. *Continental Shelf Research*, *20*(3), 313–330. https://doi.org/10.1016/s0278-4343(99)00072-2

Gopalan, A. K. S., Krishna, V. V. G., Ali, M. M., & Sharma, R. (2000). Detection of Bay of Bengal eddies from TOPEX and in situ observations. *Journal of Marine Research*, *58*(5), 721–734. https://doi.org/10.1357/002224000321358873

Gordon, A., Shroyer, E., & Murty, V. (2017). An Intrathermocline Eddy and a tropical cyclone in the Bay of Bengal. *Scientific Reports*, *7*(1), 46218. https://doi.org/10.1038/srep46218

Goswami, B. N. (2012). South Asian monsoon. In *Intraseasonal variability in the atmosphere-ocean climate system* (pp. 21–72). Springer Praxis Books. https://doi.org/10.1007/978-3-642-13914-7_2

Hastenrath, S. (1994). *Climate dynamics of the tropics: An updated edition of climate and circulation of the tropics* (p. 488). Kluwer Academic.

Hauri, C., Irving, B., Hayes, D., Abdi, E., Kemme, J., Kinski, N., & McDonnell, A. M. P. (2024). Expanding seawater carbon dioxide and methane measuring capabilities with a Seaglider. *Ocean Science*, *20*(5), 1403–1421. https://doi.org/10.5194/os-20-1403-2024

Jha, R. K., & Udaya Bhaskar, T. V. S. (2021). Optimal parameters for generation of gridded product of Argo temperature and salinity using DIVA [Dataset]. *Journal of Earth System Science*, *130*, 170. https://doi.org/10.1007/s12040-021-01675-2

Jofia, J., Girishkumar, M. S., McPhaden, M. J., & Pattabhi Ram Rao, E. (2021). Diurnal variability of atmospheric cold pool events and associated air-sea interactions in the Bay of Bengal during the summer monsoon. *Climate Dynamics*, *56*(3–4), 837–853. https://doi.org/10.1007/s00382-020-05506-w

Kara, A. B., Rochford, P. A., & Hurlburt, H. E. (2003). Mixed layer depth variability over the global ocean. *Journal of Geophysical Research*, *108*, 3079. https://doi.org/10.1029/2000jc000736

Kim, S.-B., Fukumri, I. I., & Lee, T. (2006). The closure of the ocean mixed layer temperature budget using level-coordinate model fields. *Journal of Atmospheric and Oceanic Technology*, *23*(6), 840–853. https://doi.org/10.1175/JTECH1883.1

Kumar, P. S., Muraleedharan, P. M., Prasad, T. G., Gauns, M., Ramaiah, N., Desouza, S. N., et al. (2002). Why is the BoB less productive during summer monsoon compared to the Arabian Sea? *Geophysical Research Letters*, *29*. https://doi.org/10.1029/2002GL016013

Kurian, J., & Vinayachandran, P. N. (2006). Formation mechanisms of temperature inversions in the southeastern Arabian Sea. *Geophysical Research Letters*, *33*(17), L17611. https://doi.org/10.1029/2006GL027280

Li, X. L., Cheng, X., Jing, Z., Cao, H., & Feng, T. (2022). Submesoscale motions and their seasonality in the northern Bay of Bengal. *Acta Oceanologica Sinica*, *41*(4), 1–13. https://doi.org/10.1007/s13131-021-1847-6

Li, Y., Han, W., Ravichandran, M., Wang, W., Shinoda, T., & Lee, T. (2017). Bay of Bengal salinity stratification and Indian summer monsoon intraseasonal oscillation: 1. Intraseasonal variability and causes. *Journal of Geophysical Research: Oceans*, *122*(5), 4291–4311. https://doi.org/10.1002/2017JC012691

Lin, I.-I., Chen, C.-H., Pun, I.-F., Liu, W. T., & Wu, C.-C. (2009). Warm ocean anomaly, air sea fluxes, and the rapid intensification of tropical cyclone Nargis (2008). *Geophysical Research Letters*, *36*(3), L03817. https://doi.org/10.1029/2008GL035815

Lotliker, A. A., Omand, M. M., Lucas, A. J., Laney, S. R., Mahadevan, A., & Ravichandran, M. (2016). Penetrative radiative flux in the Bay of Bengal. *Oceanography*, *29*(2), 214–221. https://doi.org/10.5670/oceanog.2016.53

Lucas, A. J., Nash, J. D., Pinkel, R., MacKinnon, J. A., Tandon, A., Mahadevan, A., et al. (2016). Adrift upon a salinity-stratified sea: A view of upper-ocean processes in the Bay of Bengal during the southwest monsoon. *Oceanography*, *29*(2), 134–145. https://doi.org/10.5670/oceanog.2016.46

MacKinnon, J. A., Nash, J. D., Alford, M. H., Lucas, A. J., Mickett, J. B., Shroyer, E. L., et al. (2016). A tale of two spicy seas. *Oceanography*, *29*(2), 50–61. https://doi.org/10.5670/oceanog.2016.38

Mahadevan, A., Spiro Jaeger, G., Freilich, M., Omand, M., Shroyer, E. L., & Sengupta, D. (2016). Freshwater in the Bay of Bengal: Its fate and role in air-sea heat exchange. *Oceanography*, *29*(2), 72–81. https://doi.org/10.5670/oceanog.2016.40

McKie, T., Lucas, A. J., & MacKinnon, J. (2024). Submesoscale dynamics in the Bay of Bengal: Inversions and instabilities. *Journal of Geophysical Research: Oceans*, *129*(3), e2023JC020563. https://doi.org/10.1029/2023JC020563

McPhaden, M. J., Foltz, G. R., Lee, T., Murty, V. S. N., Ravichandran, M., Vecchi, G. A., et al. (2009). Ocean-atmosphere interactions during cyclone nargis. *EOS, Transactions American Geophysical Union*, *90*(7), 53–54. https://doi.org/10.1029/2009EO070001

McWilliams, J. C. (2016). Submesoscale currents in the ocean. *Proceedings of the Royal Society A: Mathematical, Physical and Engineering Sciences*, *472*(2189), 20160117. https://doi.org/10.1098/rspa.2016.0117

Meissner, T., Wentz, F. J., Manaster, A., Lindsley, R., Brewer, M., & Densberger, M. (2022). Remote Sensing Systems SMAP Ocean Surface Salinities [Level 2C, Level 3 Running 8- day, Level 3 Monthly], Version 5.0 validated release [Dataset]. *Remote Sensing Systems*. Retrieved from www.remss.com/missions/smap

Morel, A., & Antoine, D. (1994). Heating rate within the upper ocean in relation to its bio–optical state. *Journal of Physical Oceanography*, *24*(7), 1652–1665. https://doi.org/10.1175/1520-0485(1994)024<1652:HRWTUO>2.0.CO;2

Orenstein, P., Fox-Kemper, B., Johnson, L., Li, Q., & Sane, A. (2022). Evaluating coupled climate model parameterizations via skill at reproducing the monsoon intraseasonal oscillation. *Journal of Climate*, *35*(6), 1873–1884. https://doi.org/10.1175/jcli-d-21-0337.1

Pant, V., Girishkumar, M. S., Bhaskar, T. U., Ravichandran, M., Papa, F., & Thangaprakash, V. P. (2015). Observed interannual variability of near-surface salinity in the Bay of Bengal. *Journal of Geophysical Research: Oceans*, *120*(5), 3315–3329. https://doi.org/10.1002/2014JC010340

Papa, F., Durand, F., Rossow, W. B., Rahman, A., & Bala, S. K. (2010). Satellite altimeter-derived monthly discharge of the Ganga-Brahmaputra River and its seasonal to interannual variations from 1993 to 2008. *Journal of Geophysical Research*, *115*(C12), C12013. https://doi.org/10.1029/2009JC006075

Parampil, S. R., Gera, A., Ravichandran, M., & Sengupta, D. (2010). Intraseasonal response of mixed layer temperature and salinity in the BoB to heat and freshwater flux. *Journal of Geophysical Research*, *115*, C05002. https://doi.org/10.1029/2009JC005790

Paul, N., Sukhatme, J., Sengupta, D., & Gayen, B. (2021). Eddy-induced trapping and homogenization of freshwater in the Bay of Bengal. *Journal of Geophysical Research: Oceans*, *126*(6), e2021JC017180. https://doi.org/10.1029/2021JC017180

Pham, H. T., Sarkar, S., Johnson, L., Fox-Kemper, B., Sullivan, P. P., & Li, Q. (2023). Multi-scale temporal variability of turbulent mixing during a Monsoon Intra-seasonal Oscillation in the Bay of Bengal: An LES study. *Journal of Geophysical Research: Oceans*, *128*(1), e2022JC018959. https://doi.org/10.1029/2022JC018959

Pickard, G. L., & Emery, W. J. (1990). *Descriptive physical oceanography: An introduction* (5th ed.). Butterworth-Heinemann.

Pramanik, S., Sil, S., Mandal, S., Dey, D., & Shee, A. (2019). Role of interannual equatorial forcing on the subsurface temperature dipole in the Bay of Bengal during IOD and ENSO events. *Ocean Dynamics*, *69*(11–12), 1253–1271. https://doi.org/10.1007/s10236-019-01303-0

Prasad, T. G. (2004). A comparison of mixed layer dynamics between the Arabian Sea and the BoB: One-dimensional model results. *Journal of Geophysical Research*, *109*, C03035. https://doi.org/10.1029/2003JC002000

PrasannaKumar, S., Unnikrishnan, A. S., & Muraleedharan, P. M. (2000). Signatures of Kelvin and Rossby wave propagation in the northern Indian Ocean from TOPEX/POSEIDON Altimeter. In *The Fifth Pacific Ocean remote sensing conference (PORSEC), 5–8 December 2000. Proceedings* (Vol. 1, pp. 276–279). Retrieved from http://drs.nio.org/drs/handle/2264/1703

Prend, C. J., Seo, H., Weller, R. A., & Farrar, J. T. (2019). Impact of freshwater plumes on intraseasonal upper ocean variability in the Bay of Bengal. *Deep Sea Research Part II: Topical Studies in Oceanography*, *161*, 63–71. https://doi.org/10.1016/j.dsr2.2018.09.007

Ramachandran, S., & Tandon, A. (2020). Generation of submesoscale temperature inversions below salinity fronts in the Bay of Bengal. *Journal of Geophysical Research: Oceans*, *125*(12), e2020JC016278. https://doi.org/10.1029/2020JC016278

Ramachandran, S., Tandon, A., Mackinnon, J., Lucas, A. J., Pinkel, R., Waterhouse, A. F., et al. (2018). Submesoscale processes at shallow salinity fronts in the Bay of Bengal: Observations during the winter monsoon. *Journal of Physical Oceanography*, *48*(3), 479–509. https://doi.org/10.1175/JPO-D-16-0283.1

Rao, R. R., Girish Kumar, M. S., Ravichandran, M., Rao, A. R., Gopalakrishna, V. V., & Thadathil, P. (2010). Interannual variability of Kelvin wave propagation in the wave guides of the equatorial Indian Ocean, the coastal Bay of Bengal and the southeastern Arabian Sea during 1993–2006. In *Deep Sea Research Part I: Oceanographic Research Papers* (Vol. 57(1), pp. 1–13). https://doi.org/10.1016/j.dsr.2009.10.008

Rao, R. R., & Sivakumar, R. (2000). Seasonal variability of near-surface thermal structure and heat budget of the mixed layer of the tropical Indian Ocean from a new global ocean temperature climatology. *Journal of Geophysical Research*, *105*(C1), 995–1016. https://doi.org/10.1029/1999jc900220

Rao, R. R., & Sivakumar, R. (2003). Seasonal variability of sea surface salinity and salt budget of the mixed layer of the north Indian Ocean. *Journal of Geophysical Research*, *108*(C1). https://doi.org/10.1029/2001jc000907

Rudnick, D. L., & Martin, J. P. (2002). On the horizontal density ratio in the upper ocean. *Dynamics of Atmospheres and Oceans*, *36*(1–3), 3–21. https://doi.org/10.1016/s0377-0265(02)00022-2

Sandeep, K. K., Pant, V., Girishkumar, M. S., & Rao, A. D. (2018). Impact of riverine freshwater forcing on the sea surface salinity simulations in the Indian Ocean. *Journal of Marine Systems*, *185*, 40–58. https://doi.org/10.1016/j.jmarsys.2018.05.002

Schmid, C., Molinari, R. L., Sabina, R., Daneshzadeh, Y.-H., Xia, X., Forteza, E., & Yang, H. (2007). The real-time data management system for Argo profiling float observations [Software]. *Journal of Atmospheric and Oceanic Technology*, *24*(9), 1608–1628. https://doi.org/10.1175/jtech2070.1

Sengupta, D., Bharath Raj, G. N., Ravichandran, M., Sree Lekha, J., & Papa, F. (2016). Near-surface salinity and stratification in the North Bay of Bengal from moored observations. *Geophysical Research Letters*, *43*(9), 4448–4456. https://doi.org/10.1002/2016GL068339

Sengupta, D., Bharath Raj, G. N., & Shenoi, S. S. C. (2006). Surface freshwater from the Bay of Bengal runoff and the Indonesian throughflow in the tropical Indian Ocean. *Geophysical Research Letters*, *33*(22), L22609. https://doi.org/10.1029/2006gl027573

Sengupta, D., Goddalehundi, B. R., & Anitha, D. S. (2008). Cyclone-induced mixing does not cool SST in the post-monsoon North Bay of Bengal. *Atmospheric Science Letters*, *9*, 1–6. https://doi.org/10.1002/asl.162

Sengupta, D., & Ravichandran, M. (2001). Oscillations of Bay of Bengal Sea surface temperature during the 1998 summer monsoon. *Geophysical Research Letters*, *28*(10), 2033–2036. https://doi.org/10.1029/2000gl012548

Shankar, D., Vinayachandran, P. N., & Unnikrishnan, A. S. (2002). The monsoon currents in the north Indian Ocean. *Progress in Oceanography*, *52*(1), 63–120. https://doi.org/10.1016/s0079-6611(02)00024-1

Shenoi, S. S. C., Shankar, D., & Shetye, S. R. (2002). Differences in heat budgets of the near-surface Arabian Sea and BoB: Implications for the summer monsoon. *Journal of Geophysical Research*, *107*(C6), 3052. https://doi.org/10.1029/2000JC000679

Sherin, V. R., Girishkumar, M. S., Shivaprasad, S., Sureshkumar, N., Farrar, J. T., Athulya, K., et al. (2023). Importance of seasonally evolving near-surface salinity stratification on mixed layer heat budget during Summer Monsoon Intraseasonal Oscillation in the northern Bay of Bengal in 2019. *Journal of Geophysical Research: Oceans*, *128*(11), e2023JC019800. https://doi.org/10.1029/2023JC019800

Shroyer, E., Tandon, A., Sengupta, D., Fernando, H. J., Lucas, A. J., Farrar, J. T., et al. (2021). Bay of Bengal intraseasonal oscillations and the 2018 monsoon onset. *Bulletin of the American Meteorological Society*, *102*(10), E1936–E1951. https://doi.org/10.1175/bams-d-20-0113.1

Shroyer, E. L., Gordon, A. L., Jaeger, G. S., Freilich, M., Waterhouse, A. F., Farrar, J. T., et al. (2020). Upper-layer thermohaline structure of the Bay of Bengal during the 2013 northeast monsoon. *Deep Sea Research Part II: Topical Studies in Oceanography*, *172*, 104630. https://doi.org/10.1016/j.dsr2.2019.07.018

Shroyer, E. L., Rudnick, D. L., Farrar, J. T., Lim, B., Venayagamoorthy, S. K., St. Laurent, L. C., et al. (2016). Modification of upper-ocean temperature structure by subsurface mixing in the presence of strong salinity stratification. *Oceanography*, *29*(2), 62–71. https://doi.org/10.5670/oceanog.2016.39

Simoes-Sousa, I. T., Tandon, A., Buckley, J., Sengupta, D., Shroyer, E., & de Szoeke, S. P. (2022). Atmospheric cold pools in the Bay of Bengal. *Journal of the Atmospheric Sciences*, *80*, 167–180. https://doi.org/10.1175/JAS-D-22-0041.1

Sree Lekha, J., Buckley, J., Tandon, A., & Sengupta, D. (2018). Subseasonal dispersal of freshwater in the northern Bay of Bengal in the 2013 summer monsoon season. *Journal of Geophysical Research: Oceans*, *123*(9), 6330–6348. https://doi.org/10.1029/2018JC014181

Sree Lekha, J., Lucas, A. J., Sukhatme, J., Joseph, J. K., Ravichandran, M., Suresh Kumar, N., et al. (2020). Quasi-Biweekly mode of the Asian summer monsoon revealed in Bay of Bengal surface observations. *Journal of Geophysical Research: Oceans*, *125*(12), e2020JC016271. https://doi.org/10.1029/2020JC016271

Sreelekha, J., & McPhaden, M. J. (2022). Ocean mixed layer response to two post-monsoon cyclones in the Bay of Bengal in 2018. *Journal of Geophysical Research: Oceans*, *127*(9), e2022JC018874. https://doi.org/10.1029/2022JC018874

Sweeney, C., Gnanadesikan, A., Griffies, S. M., Harrison, M. J., Rosati, A. J., & Samuels, B. L. (2005). Impacts of shortwave penetration depth on large-scale ocean circulation and heat transport. *Journal of Physical Oceanography*, *35*(6), 1103–1119. https://doi.org/10.1175/JPO2740.1

Taylor, J. R., & Thompson, A. F. (2023). Submesoscale dynamics in the upper ocean. *Annual Review of Fluid Mechanics*, *55*(1), 103–127. https://doi.org/10.1146/annurev-fluid-031422-095147

Thadathil, P., Gopalakrishna, V. V., Muraleedharan, P. M., Reddy, G. V., Araligidad, N., & Shenoy, S. (2002). Surface layer temperature inversion in the Bay of Bengal. *Deep-Sea Research*, *49*(10), 1801–1818. https://doi.org/10.1016/s0967-0637(02)00044-4

Thadathil, P., Muraleedharan, P. M., Rao, R. R., Somayajulu, Y. K., Reddy, G. V., & Revichandran, C. (2007). Observed seasonal variability of barrier layer in the BoB. *Journal of Geophysical Research*, *112*, C02009. https://doi.org/10.1029/2006JC003651

Thadathil, P., Suresh, I., Gautham, S., Prasanna Kumar, S., Lengaigne, M., Rao, R. R., et al. (2016). Surface layer temperature inversion in the Bay of Bengal: Main characteristics and related mechanisms. *Journal of Geophysical Research: Oceans*, *121*(8), 5682–5696. https://doi.org/10.1002/2016JC011674

Thangaprakash, V. P., Girishkumar, M. S., Suprit, K., Suresh, N., Dipanjan, D., Ashok, K., et al. (2016). What controls seasonal evolution of SST in the Bay of Bengal? Mixed layer heat budget analysis using moored buoy observations along 90°E. *Oceanography*, *29*(2), 202–213. https://doi.org/10.5670/oceanog.2016.52

Thangaprakash, V. P., Girishkumar, M. S., Sureshkumar, N., Ravichandran, M., Naidu, C. V., Ramakrishna, S. S. V. S., & Sahoo, A. (2025). Mixed layer salinity budget in the Northern Bay of Bengal using the data from a mooring array in 2015. *Ocean Dynamics*, *75*(5), 40. https://doi.org/10.1007/s10236-025-01681-8

UW. (2013). Seaglider quality control manual for basestation 2.08 (Tech. rep.). Seattle, WA: School of Oceanography and Applied Physics Laboratory [Software]. *University of Washington*. Retrieved from http://gliderfs2.coas.oregonstate.edu/sgliderweb/Seaglider_Quality_Control_Manual.html

Vecchi, G. A., & Harrison, D. E. (2002). Monsoon breaks and subseasonal sea surface temperature variability in the Bay of Bengal. *Journal of Climate*, *15*(12), 1485–1493. https://doi.org/10.1175/1520-0442(2002)015<1485:MBASSS>2.0.CO;2

Venkatesan, R., Shamji, V. R., Latha, G., Mathew, S., Rao, R. R., Muthiah, A., & Atmanand, M. A. (2013). In situ ocean subsurface time-series measurements from OMNI buoy network in the Bay of Bengal [Dataset]. *Current Science*, *104*, 1166–1177. https://www.jstor.org/stable/24092396

Vialard, J., Foltz, G. R., McPhaden, M. J., Duvel, J. P., & de Boyer Montégut, C. (2008). Strong Indian Ocean sea surface temperature signals associated with the Madden-Julian Oscillation in late 2007 and early 2008. *Geophysical Research Letters*, *35*(19), L19608. https://doi.org/10.1029/2008GL035238

Vinayachandran, P. N., Murty, V. S. N., & Ramesh Babu, V. (2002). Observations of barrier layer formation in the BoB during summer monsoon. *Journal of Geophysical Research*, *107*(C12), 8018. https://doi.org/10.1029/2001JC000831

Weller, R. A., Farrar, J. T., Buckley, J., Mathew, S., Venkatesan, R., Sree Lekha, J., et al. (2016). Air-sea interaction in the Bay of Bengal. *Oceanography*, *29*(2), 28–37. https://doi.org/10.5670/oceanog.2016.36

Weller, R. A., Farrar, J. T., Seo, H., Prend, C., Sengupta, D., Sree Lekha, J., et al. (2019). Moored observations of the surface meteorology and air-sea fluxes in the northern Bay of Bengal in 2015. *Journal of Climate*, *32*(2), 549–573. https://doi.org/10.1175/JCLI-D-18-0413.1

Wilson, E., & Riser, S. (2016). An assessment of the seasonal salinity budget for the upper BoB. *Journal of Physical Oceanography*, *46*(5), 1361–1376. https://doi.org/10.1175/JPO-D-15-0147.1

Yu, L. (2003). Variability of the depth of the 20°C isotherm along 6°N in the Bay of Bengal: Its response to remote and local forcing and its relation to satellite SSH variability. *Deep-Sea Research Part II*, *50*(12–13), 2285–2304. https://doi.org/10.1016/s0967-0645(03)00057-2

Yu, L., O'Brien, J. J., & Yang, J. (1991). On the remote forcing of the circulation in the Bay of Bengal. *Journal of Geophysical Research*, *96*, 20449–20454.